11-30-2020

# Sub-pixel Sensitivity Variations and their Effects on Precision Aperture Photometry

Alexis M. Irwin
lmi3968@rit.edu

# Sub-pixel Sensitivity Variations and their Effects on Precision Aperture Photometry

Alexis M. Irwin

A Thesis Submitted in Partial Fulfillment of the Requirements for the Degree of Master of Science in Imaging Science

Chester F. Carlson Center for Imaging Science
College of Science
Rochester Institute of Technology
Rochester, NY
November 30, 2020

Approved by: _____

Charles Bachmann, Ph.D. Date

M.S. Program Coordinator, Imaging Science

Approval Committee: Zoran Ninkov, Dmitry Vorobiev, Joel Kastner

Chester F. Carlson Center for Imaging Science
College of Science
Rochester Institute of Technology
Rochester, NY

CERTIFICATE OF APPROVAL

---

**M.S. DEGREE THESIS**

The M.S. Degree Thesis of Alexis M. Irwin
has been examined and approved by the thesis
committee as satisfactory for the thesis
requirement for the M.S. degree in
Imaging Science.

---

Dr. Zoran Ninkov, Thesis Advisor

---

Dr. Dmitry Vorobiev

---

Dr. Joel Kastner

Date

# Contents

## Abstract

The response of pixels in CCDs and CMOS arrays is not uniform; physical aspects of pixel structure can create non-uniform electric fields within a pixel and the diffusion of carriers tends to blur pixel boundaries. It has previously been shown that the sub-pixel response can vary by up to 50% across a pixel, with more light being detected near the center and less around the edges. This intra-pixel response function (IPRF) can have significant effects on the aperture photometry of under-sampled PSFs, like those found in the *Kepler* and TESS exoplanet hunting missions. Knowledge of the IPRF can be used to correct for systematic variations in photometric measurements introduced by the sub-pixel variations in response. Additionally, in systems for which the optical PSF is not well defined, knowledge of the IPRF can allow for extraction of the optical PSF.

Presented here are the results of the direct measurement of the IPRF of a thinned, back-illuminated CCD of the same model used on the NASA *Kepler* mission. The experimental setup used to measure the IPRF is discussed in detail. Measurements of the IPRF were made at various wavelengths, then combined to create an "effective IPRF" for the broad spectral bandpass filter used for collecting the scientific data of interest. This effective IPRF was then utilized in a model to study the effects of the IPRF on time series aperture photometry. The effects of spacecraft jitter and drift on aperture photometry were also investigated. Such results are relevant for exoplanet searches using the photometric detection technique as implemented in the *Kepler* and TESS missions.

# 1. INTRODUCTION

Humans have been estimating the brightness of stars for millennia. Ptolemy's work *Almagest*, completed around 150 CE, contains the earliest record of stellar coordinates and their relative brightness that still exists today;[1] however, it is often noted that Ptolmy's work likely builds off of the work of Hipparchus who died around 120 BCE. Ptolemy recorded the relative brightness of stars by sorting them into 6 magnitude classes, the first magnitude containing the brightest stars, and the sixth magnitude containing the dimmest stars visible to the naked eye. This magnitude system was used for centuries, and formed the basis for the magnitude system which is still used by astronomers today.

Despite how early in human history the first estimates of stellar brightness were made, it wasn't until the late 1700s that anyone performed what could be considered *stellar photometry* in the modern sense. William Hershel was the first to apply scientific methods to the measurement of stellar brightness, and he did so with the purpose of determining stellar variability. He used what later became known as the "step method" to record the relative brightness of stars near each other in the sky. He was capable of achieving an estimated precision of $\pm 0.17$ mag using by-eye measurements.[2]

In the mid to late 1800s many devices, called visual photometers, were designed to help aid in by-eye photometric measurements. Many of these devices worked by bringing two stars that were distant on the sky, one of them usually a standard star, next to each other in a common focal plane so they could be compared side-by-side. Others used a neutral glass wedge placed in the eyepiece of a telescope. The wedge was moved until the star of interest was extincted, and the position of the wedge was read off and could be converted to a stellar magnitude.[3] The most accurate visual photometers used the polarization of light to determine magnitudes, and resulted in an error of about a tenth of a magnitude, not much better than a skilled observer without the aid of a photometer.[4]

The popularity of these devices only lasted for about a half a century before the use of photographic plates became the go-to method for photometry. One of the first large scale photographic astronomical surveys was conducted at Harvard by Edward Pickering starting in 1885, but the photometric accuracy achieved was lower than was possible with visual methods. Still, photography showed promise for use in astronomy due to its ability to capture images of many stars at once and its sensitivity to UV and

x-ray photons.[5] It wasn't until about 1930 that the precision achieved using photography became significantly better than what was capable with the human eye, measuring magnitudes with a precision of approximately $\pm 0.02$ mag.[2]

The rise in popularity of photoelectric photometers, the most common type being photomultiplier tubes (PMTs), allowed for the detection of stars fainter than ever before, as well as the ability to perform high-speed time-series photometry. PMTs had the advantage of much higher sensitivity to light than photographic techniques, as well as exhibiting a linear response to light. Braddick reported in 1960 that the average quantum efficiency of a PMT was $\sim 30\%$, but up to 50% was possible,[6] while photographic methods had quantum efficiencies $\leq 1.0\%$. To perform photometry with PMTs, the photometer was connected to the telescope such that the focal plane was located within the PMT. Often, a wheel containing aperture of different sizes was placed in front of the PMT, and the aperture size was selected to maximize the amount of light from the star, while minimizing the contribution of background light.[7] Unfortunately, only one star at a time could be observed using this method.

Most recently, CCDs have revolutionized astronomy and allowed for unprecedented photometric precision. Similar to PMTs, CCDs exhibit high sensitivity over a wide range of wavelengths and a linear response to light. High speed photometry is more difficult with CCDs,[8] but the ability to capture and analyze many stars in one frame has made them the detector of choice for astronomers since the 1980s. The two most important methods for stellar photometry with CCDs are aperture photometry and PSF fitting, which are discussed section 2. A more complete history of stellar photometry is given by Miles.[2]

Modern space-based missions like *Kepler* and TESS have lead to an increased understanding of exoplanets and stellar variability via use of advanced photometry methods, and have achieved photometric precision on the order of 10 parts-per-million for the brightest stars observed.[9,10] We are now reaching a point where the photometric precision we are capable of achieving is limited by spacecraft performance, as well as our understanding of some of the fundamental aspects of CCDs themselves such as sub-pixel sensitivity variations.

The goal of the work presented in this thesis is to measure the sub-pixel sensitivity variations of a back-illuminated CCD, called the intra-pixel response function (IPRF), and to use this measurement to better understand the effects of sub-pixel sensitivity variations on aperture photometry under different observing conditions. Measuring the

IPRF for a detector can lead to improved photometric precision. Also, in situations where the optical PSF is unknown, the IPRF can be used to determine it, allowing for the use of PSF fitting for photometry. By determining how the IPRF affects photometry for various amounts of spacecraft jitter and drift, it becomes easier to disentangle these effects from actual differences in signal due to stellar variability and planetary transits, and *a priori* knowledge of the sub-pixel variations can be used to improve detrending methods in the data reduction pipeline, possibly leading to new scientific discoveries.

# 2. MODERN METHODS FOR PHOTOMETRY

Distant stars are point sources when viewed from the vicinity of Earth; however, due to the optics of telescopes, as well as atmospheric effects when observed from Earth's surface, a star's light ends up being spread out and having some physical shape when recorded. The observed shape, or profile, of the star due to these effects is called the point-spread function (PSF). The optical PSF of a telescope can vary across the field of view; however, for any star located in the same region of the field of view, the shape of the PSF will generally be the same regardless of magnitude. This is important for the two main photometry methods used on CCD images discussed here, aperture photometry and PSF fitting.

## 2.1 Aperture Photometry

Aperture photometry of CCD images is similar to photometry performed with photoelectric photometers as described briefly in section 1, with the physical aperture replaced by a virtual aperture made up of CCD pixels. In general, an aperture containing an object of interest is chosen, and the signal of the pixels within the aperture is summed. An annulus of pixels centered on this aperture is also analyzed to determine the contribution of background light to the recorded signal within the aperture. The background signal per pixel in the annulus is calculated, multiplied by the number of pixels that make up the source aperture, and subtracted from the source aperture signal, giving the value of the light from the source only. The basic equation for aperture photometry is,

$$S_{src} = S_{ap} - B_{pp} \cdot n_{ap}, \tag{1}$$

where $S_{src}$ is the signal from the source only, $S_{ap}$ is all of the signal within the summed aperture, $B_{pp}$ is the average background signal per pixel in the annulus, and $n_{ap}$ is the number of pixels within the aperture. An example of a typical circular aperture and annulus are shown in figure 1.

While this process seems trivial at first, the wide extent of the wings of the PSF present two main issues in performing aperture photometry. First, as the aperture radius increases, the light from the star eventually becomes so diffuse that read noise and noise due to background signal begin to increase more rapidly than the source signal making the signal at large radii impossible to measure. Second, stars are not isolated on the sky. Light from other sources often contaminates the signal in the tails of the PSF of

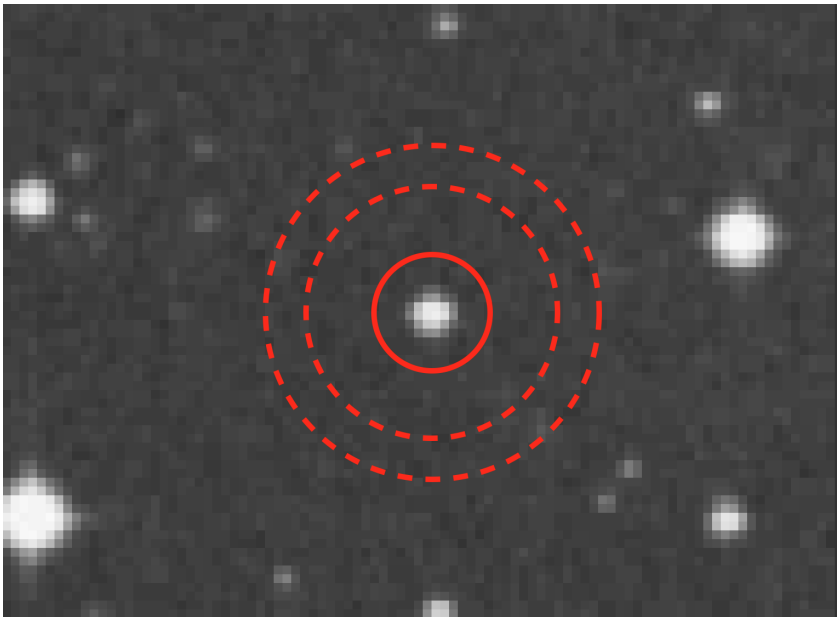

Figure 1: Example of aperture (solid circle) and annulus (dashed circles). Image Credit: AURA.

the star of interest or the signal within the background annulus. Therefore, attempting to count up *all* of a star's light is unreasonable, and apertures must be selected such that noise and nearby sources do not become problematic.

To avoid these issues, apertures should be selected such that the signal-to-noise ratio (SNR) of the aperture photometry is maximized for each star being measured.[11] In general, the selected apertures tend to be larger for brighter stars and smaller for dimmer stars. This often means that a significant percentage of the source signal is located outside of the selected aperture. If the goal of aperture photometry is precise determination of the object's standardized magnitude, it is important to attempt to account for all light from the source. In other cases, the absolute photometry is not important, and relative aperture photometry is used instead.

### 2.1.1 Absolute Aperture Photometry

With absolute aperture photometry, the goal is to account for all detectable signal from a star and translate that signal to a standard magnitude value. This can be accomplished using the growth curve method and standard stars (i.e. stars for which the magnitude is already well known).

Growth curves are created by calculating the sum of source signal within apertures of increasing radii for bright, isolated stars in the frame, then plotting the difference

in collected signal for each radius size and fitting a curve to the data. An example growth curve is shown in figure 2. From the curve of growth, the percentage of *detectable* light within a certain radius can be found, this will be the same percentage for all sources with the same PSF regardless of magnitude.

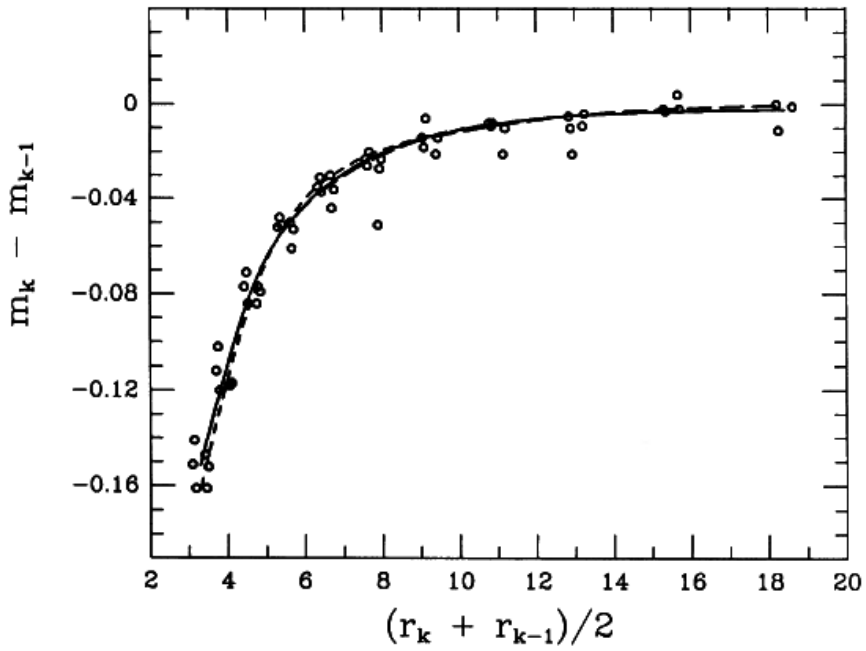


Figure 2: An example of a growth curve adapted from Stetson.[12] The points are the actual magnitude differences calculated for various sources in the observed field, and the solid and dashed lines show different fits to the data.

Based on the sum of the signal within a small radius containing only the brightest pixels, the total detectable signal from the source can be determined. If the PSF is known to vary across the field of view, growth curves will need to be created for different areas, and used to correct only those stars nearby. After correcting to obtain the total detectable flux from the star, standard stars are used to convert the flux from the star to a standard magnitude. Because the magnitudes of the standard stars are already known, performing aperture photometry on these stars along with the stars to be measured allows a conversion to standard magnitudes to be applied to all stars of interest.

Growth curves are also important for deciding the location of the annulus. Because the annulus is used to determine the background signal, its inner radius should be larger than the radius at which the growth curve reaches plateau. This can be difficult for crowded fields in which case apertures far enough away from the star of interest

may be contaminated by light from neighboring stars. In these cases, PSF fitting is the preferred method. A detailed discussion of the growth curve method is given by Stetson.[12]

### 2.1.2 Relative Aperture Photometry

Aperture photometry can also be used to measure not the precise, standardized magnitude of the source, but small changes in a star's brightness over time. This is achieved through time-series aperture photometry.[13,14] For this method, a series of many exposures of the same field are taken, and aperture photometry is performed on each. In this case, stars with small apertures do not need to have corrections performed on them, and the magnitudes observed do not need to be standardized, instrumental magnitudes are fine. The main concern in this method of aperture photometry is to achieve the highest SNR possible for each measurement or set of measurements.

Often in this case, differential aperture photometry is used to further increase photometric precision. With differential photometry, trends over time for all measured stars in the field of view are analyzed and trends that are common across all stars in the field are removed from the data. This decreases systematic errors in the final aperture photometry, such as those due to spacecraft jitter or pointing drift.

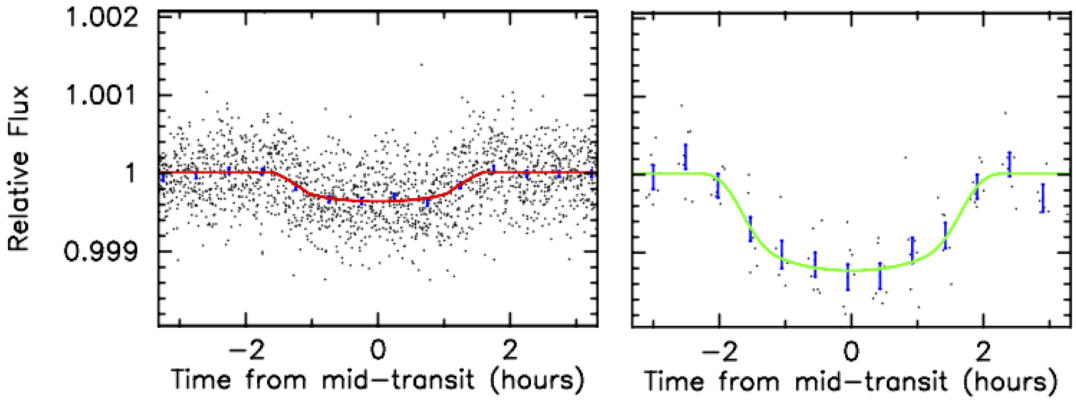


Figure 3: An example of processed light curves for two confirmed exoplanet transits discovered by the *Kepler* mission. The black points are aperture photometry results for individual frames, the blue dots are the result of data binned over 30 minutes with $1\sigma$ uncertainty, and the solid lines are fits to the data. Adapted from Rowe *et al.* (2014).[15]

The results of the aperture photometry are then plotted as a function of time (or phase) and fit to create light curves. Changes in stellar brightness are observed as dips or bumps in this light curve and can indicate stellar variability, eclipsing binaries, and

exoplanet transits. Example light curves for exoplanet transits are shown in figure **??**. More detailed discussions and reviews of the methods used for aperture photometry are given by Howell[16] and DaCosta.[17]

## 2.2 PSF Fitting

Aperture photometry, along with the curve of growth method, works quite well in many cases, but has one major weakness. It is impossible to perform aperture photometry in very crowded fields because even with the use of small apertures, crowding contaminates the signal of interest within apertures. If the signal at the center of the PSF is contaminated, it is not possible to accurately determine the total magnitude of the star using the growth curve method. Instead, PSF fitting must be used.

PSF fitting uses the knowledge that for regions in a field of view where the PSF is the same, a PSF can be determined using more isolated stars, then scaled to fit stars that suffer from issues due to crowding. The PSF calculated from bright, isolated stars can be used to fit PSFs to all objects in the image based on the signal in only a few pixels in the central region of the star to predict the total signal from a source, even if crowding would make it impossible with aperture photometry.

This method is not without its own disadvantages. In many cases, it is difficult to accurately fit the tails of the PSF, which can lead to increased error in magnitude measurements.[12] Also, in situations where stars are well sampled, a PSF fit can be estimated from the image without prior knowledge of the optical PSF of the telescope. However, as is the case for many wide-field surveys, *when the PSF is undersampled, small scale structure of the PSF cannot be resolved.* In these cases, the optical PSF of the telescope must be determined using other methods before PSF fitting can occur.

Some groups have tried to reconstruct the PSF of various telescopes that suffer from undersampling by taking many images dithered by sub-pixel steps to create a super-sampled image that can recover the fine-scale detail.[18–20] Another approach involves directly measuring the sub-pixel sensitivity variations of the detector being used to determine the intra-pixel response function (IPRF), and deconvolving the IPRF from the pixel response function (PRF) observed in images to determine the optical PSF of the telescope. This is discussed further in section 4.1.

## 2.3 The Use of Aperture Photometry in Exoplanet Search Missions

Space-based exoplanet search missions such as *Kepler* and TESS use the transit method to detect planets around other stars. When viewed from the correct angle, a planet will appear to pass in front of its host star at regular intervals. When this happens, a small amount of the star's light is blocked by the planet. If this periodic change in brightness can be detected, the presence of a planet can be inferred as well as the size of the planet and its distance from the host star.

To do this, missions that detect exoplanets using the transit method perform time-series aperture photometry on images of the host star.[21–26] Time-series aperture photometry involves taking a series of exposures, performing aperture photometry on each frame, or on sets of summed frames, and using the data to create light curves for the individual stars as discussed in section 2.1. Two examples of *Kepler* light curves are shown in figure 3. The orbital period of the planet is used to determine the distance of the planet from its host star. The longer the orbital period, the farther the planet is from the star. Also, when the host star radius is known, the depth of the dip in the light curve can be used to determine the radius of the planet.

As seen in figure 3, the change in relative flux caused by a planetary transit is very small. To successfully detect a planet, it is necessary to perform very precise photometry because the amount of light blocked by the star is usually on the order of about 1% for Jupiter-sized planets, and on the order of 0.01% for Earth sized planets. For a Sun-like star this corresponds to a change in brightness of about 0.001 magnitude for a Jupiter-like planet, and about $10^{-6}$ magnitude for an Earth-like planet.

Through the selection of high SNR apertures and minimal spacecraft jitter which results in precise pointing, and by accounting for systematic errors in the data reduction pipeline, *Kepler* and TESS have been successful in their searches for exoplanets. However, because both missions, and many others like them, undersample the optical PSF of the telescope, it is likely that sub-pixel sensitivity variations will have a non-negligible affect on the resulting aperture photometry. Currently, these missions attempt to account for these variations through detrending without *a priori* knowledge of the IPRF. Knowledge of the IPRF of the detectors used in these missions can be used to improve detrending methods and increase the photometric precision, possibly resulting in an increased number of planet detections. Also, the precise optical PSF of the telescopes used

in these mission is unknown. Knowledge of the IPRF can be used to determine the PSF of these systems and allow for the use of PSF fitting, further improving the photometry.

# 3. CCD STRUCTURE AND OPERATION

The charge-coupled device (CCD) was invented in 1969 by Willard Boyle and George Smith at Bell Laboratories,[27] and first tested by Amelio, Tompsett, and Smith in 1970.[28] In the 1980s, CCDs began to be adopted by astronomers. Early CCDs were plagued by poor charge transfer efficiency (CTE) (which limited the size of the arrays) and low sensitivity to UV light. As the CTE improved, CCDs quickly revolutionized astronomy because of their linear response to light, high sensitivity across a wide spectral range, and stability.[5]

Modern scientific CCDs often have peak quantum efficiencies $\geq 90\%$, low read noise, almost perfect charge transfer efficiency (CTE), and very low dark current when sufficiently cooled, making them ideal tools for scientific applications[i]. As the performance of scientific CCDs continues to improve, and the detectors are pushed to their limits, noise sources that could once be overlooked now need to be accounted for; for example, sub-pixel variations in sensitivity.

CCD pixels are defined by gate electrodes (which create the electric field structure within a pixel that "corrall" the charge carriers) and ion implant "channel stops" (which prevent the diffusion of carriers across CCD columns). This section provides an overview of how CCDs generate and collect charge, and how diffusion and interactions with gate structures and electric fields lead to the observed variations in sensitivity within a pixel.

## 3.1 CCD Structure

Sub-pixel sensitivity variations observed in CCDs are highly dependent on the CCD design. It has been shown[29–35] that the structural features that contribute most to sub-pixel variations in sensitivity are the gate structure and whether the device is a front-illuminated CCD or a thinned, back-illuminated CCD. Diagrams of a front-illuminated and back-illuminated CCD are shown in figure 4a and 4b respectively and will be referenced throughout this section.

In general, the light collecting area of a CCD is composed of a p-type doped silicon (Si) layer, an n-type doped Si layer, a thin Si-oxide insulating layer, and the gate electronics. It is in the doped Si layers, or *epitaxial silicon*, that charge is generated. During CCD operation, all of the n-type Si and a portion, or all, of the p-type Si are

[i]Definitions and discussions of technical terms such as quantum efficiency, read noise, CTE, and dark current can be found in Janesick.[5]

fully depleted, meaning there are no free carriers present in this region. Voltages applied to the gates create electric fields within the depletion region, and a potential well within the n-type Si (the lightest areas of the shaded regions in figure 4). The $\sim$0.5 $\mu$m region in the n-layer where the potential is highest is called the *buried channel* and is where the charge is collected and transferred. The p-type Si layer is often not fully depleted; when this is the case, a field-free region exists in the p-type layer (shown by the dark shaded regions in figure 4). It is in this region that most charge diffusion will occur.

For front-illuminated CCDs, light is incident on the gate structure and must pass through the gates before being absorbed in the epitaxial Si. The gate electrodes and the p-n layers reside on a thick Silicon substrate. Charges generated in this area are not collected by the CCD because they quickly recombine with the free carriers present in the layer, and a thin electric field generated by the doping gradient between this layer and the p-doped Si layer prevent electrons from crossing the border.

Back-illuminated CCDs are illuminated on the side opposite the gate structure. Because the thick substrate layer would block most of the light, this layer and part of the p-doped Si layer are thinned away. This creates a more delicate detector, but it also improves the overall sensitivity of the CCD and allows for the detection of shorter wavelengths than is possible with front-illuminated CCDs. This is discussed further in section 3.2.

During CCD operation, voltages are applied to the gates, which creates electric fields in the Si to manipulate the charges generated by photons. How the charges interact with the electric fields created within the pixel can result in sub-pixel sensitivity variations. Since the electric fields generated are dependent on the gate structure, so are the observed sensitivity variations. In front-illuminated devices, the gates affect the sub-pixel sensitivity in an additional way, by directly absorbing some of the light; this is somewhat improved by "transparent" gate materials, like indium tin oxide (ITO). Whereas shorter wavelengths of light are most likely to be absorbed by the gates, longer wavelengths can result in interference artifacts.[29]

In the case of back-illuminated CCDs, light is incident directly on the epitaxial Si. This removes the effects caused by photon absorption in the gates as well as the effects due to interference with the gates, resulting in IPRFs that are generally more uniform at all wavelengths. However, sub-pixel sensitivity variations are still observed in back-illuminated CCDs; this is discussed further in section 4.2.

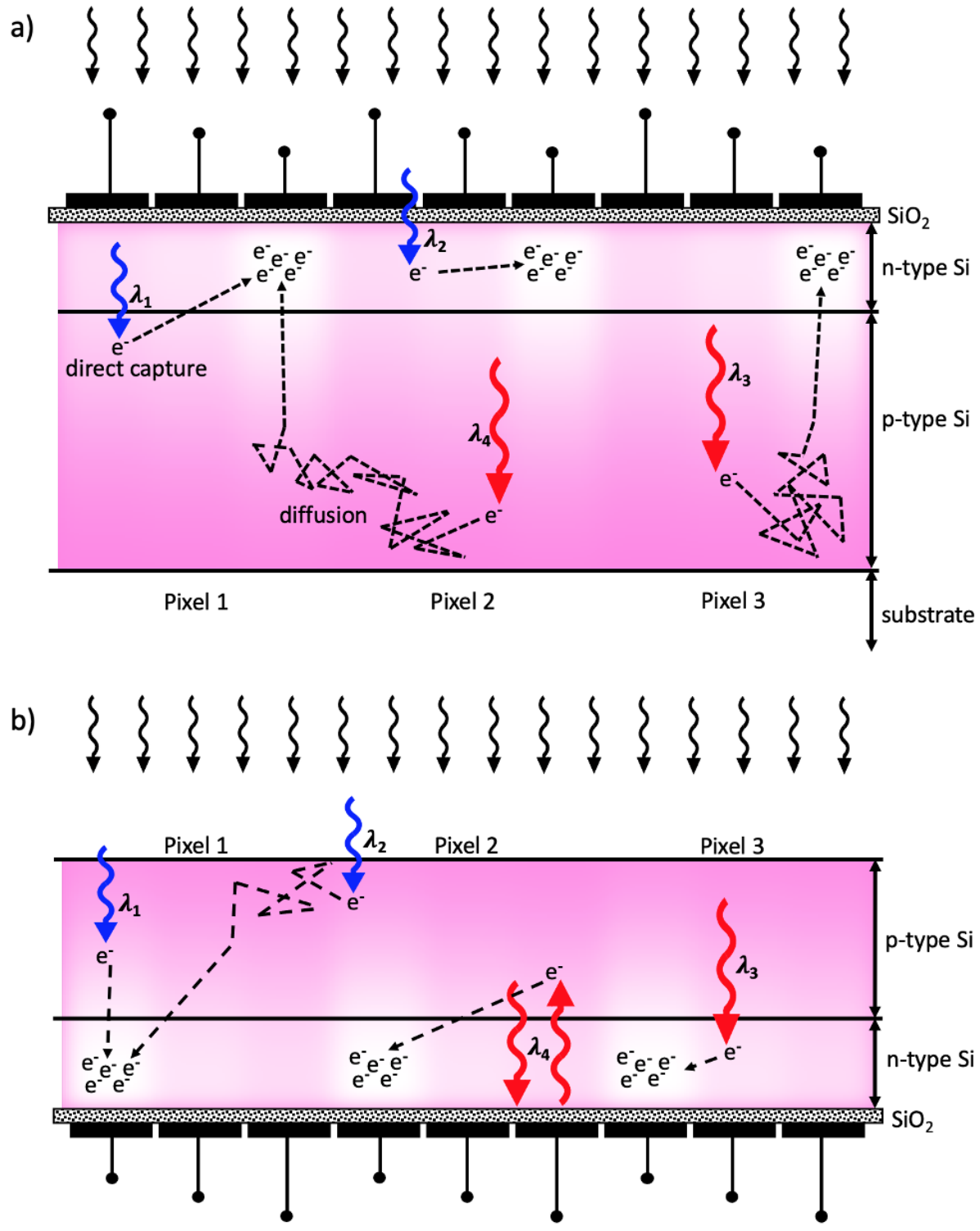


Figure 4: A 3-phase front-illuminated CCD (top) and 3-phase back-illuminated CCD (bottom). Lighter regions show areas of high potential, darker regions show the field-free region of the CCD where most diffusion occurs. Long wavelength photons are shown as red arrows, short wavelength photons are blue.

## 3.2 Charge Generation

In order to understand charge generation in CCDs, we must understand the difference between conductors, semiconductors, and insulators. Current cannot flow through insulators because the gap energy ($E_g$) between the valance band and the conduction band in these materials is so large that no, or very few, electrons ever reach the the conduction band. On the other hand, for conductors, the valence band and conduction band overlap, allowing for the presence of many free carriers and the flow of current. For semiconductors, the valence band and conduction band do not overlap, but the gap energy is such that it is relatively easy to liberate electrons from the valence band to the conduction band, generating free carriers.

When photons of the correct energy are incident on a semiconductor, atoms within the semiconductor can absorb the photon energy and release a photoelectron. In order to generate a photoelectron, a photon must have enough energy to bridge this gap energy; therefore, the gap energy determines a *cutoff wavelength* for the semiconductor, or the longest wavelength (lowest energy) photons that are capable of generating photoelectrons. This wavelength is found using the equation

$$\lambda_c = \frac{hc}{E_g}, \tag{2}$$

where $h$ is Planck's constant and $c$ is the speed of light. For silicon, $E_g = 1.13eV$ resulting in a cutoff wavelength in the near-infrared of $\lambda_c = 1100$ nm. Wavelengths longer than this cutoff wavelength will pass through the CCD without being detected.

For the purposes of explaining the features present in IPRF measurements, it is useful to understand where, in a pixel, charge is most likely to be generated for different wavelengths of light. This depends on the photon absorption depth in Si, or the distance into the Si at which 63% of the photons are absorbed. This is both wavelength and temperature dependent. The absorption depth in Si for three different temperatures across the wavelength range used to measure the IPRF in this study is shown in figure 5.

The absorption depth in Si increases as temperature decreases for all wavelengths. However, the absorption depth changes more for longer wavelengths than for shorter wavelengths for the same change in temperature. Absorption depth changes with temperature because the energy gap in Si decreases as temperature increases, so for all

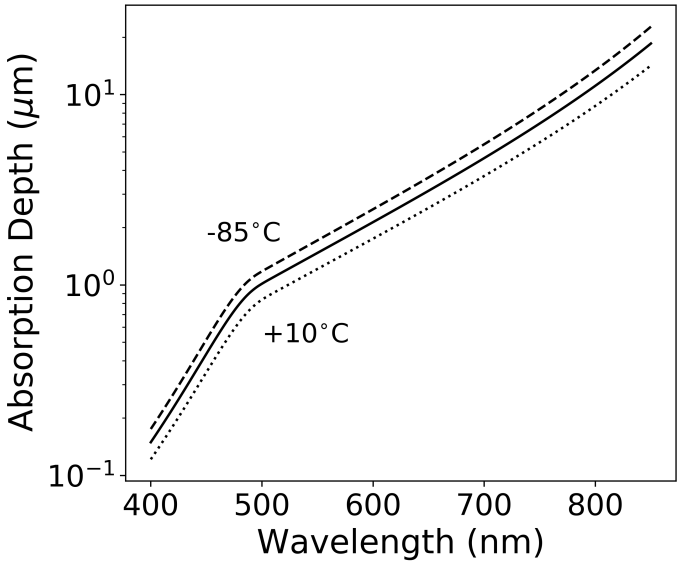


Figure 5: Absorption depth in silicon as a function of wavelength for temperatures -85°C (dashed), -45°C (solid), and +10°C (dotted). Absorption depths were calculated for the temperatures shown using the model developed by Rajkanan *et al.*[36]

wavelengths the likelihood of generating a photoelectron is greater at higher temperatures leading to a decrease in absorption depth. For Si, the energy gap varies from about 1.17 to 1.12 eV between 0-300K.[37] This temperature dependence is important to the research presented in this thesis because we operated the CCD at a higher temperature than the normal operating temperature aboard the *Kepler Space Telescope*. This is discussed further in section 5.6.

Although the temperature dependence should be considered, the wavelength dependence is more more important in explaining the features observed in measurements of sub-pixel sensitivity variations. As shown in figure 5, the absorption depth in Si for 850 nm light is on the order of 10 $\mu$m, and for 400 nm is on the order of 0.1 $\mu$m. This means that for front-illuminated CCDs, the longest wavelength photons detected are more likely to generate charge farthest from the gate structure, while the shortest wavelength photons detected generate charge very close to the gate structure (see figure 4a). The shortest wavelengths shown in figure 5 are often absorbed within the gates and never reach the silicon layer, making these wavelengths undetectable for front-illuminated CCDs. For back-illuminated CCDs photons of longer wavelengths are absorbed closer to the gates and without the gate structure in the way, the shortest wavelengths shown are detectable for these CCDs. Where charge is generated is impor-

tant in discussions regarding diffusion and interaction with the electric fields within a pixel during charge collection.

## 3.3 Charge Collection

During integration of a 3-phase CCD, one of the three gates in each pixel is held at a higher voltage than the other two. Photoelectrons generated in the depletion region (light areas in figure 4) under any of the gate structures will be swept into the region of highest potential where they are collected and held until the integration is complete. For a front-illuminated CCD this is more likely to occur for charge generated by short wavelength photons as shown by $\lambda_1$ and $\lambda_2$ in figure 4a. For back-illuminated CCDs, this is more likely to occur for charge generated by long wavelength photons, but because the device is thinned, it is more likely for short wavelength light to generate photons in this region as well ($\lambda_1$ in figure 4b).

Photoelectrons generated in the field-free regions of the CCD (dark regions in figure 4) will diffuse via a random walk and meet 1 of 3 fates: 1) the photoelectron recombines before reaching the depletion region and is not detected; 2) the photoelectron diffuses into the depletion region of the pixel in which it was generated ($\lambda_3$ in figure 4a); 3) the photoelectron diffuses into the depletion region of a neighboring pixel and is detected there ($\lambda_4$ in figure 4a and $\lambda_2$ in figure 4b). The third case is a form of cross-talk between pixels due to the diffusion of carriers.

As discussed in section (3.2), for back-illuminated CCDs such as the one used to measure the IPRF in this study, short wavelength photons are more likely to generate charges far from the gates, within the field-free region of the silicon. Notice that the depletion region extends farther from the gate held at the highest potential, than the low potential gates. This means that shorter wavelength photons are more likely to diffuse into neighboring pixels. Longer wavelength photons that generate charge closer to the gates, within the depletion region, are much less likely to diffuse. Also, for a thinned device there is a possibility that long wavelength photons will make it all the way through the depletion region without generating charge. Some of these photons may be lost, but others can be reflected off the gates back into the silicon and have a second chance to be absorbed ($\lambda_4$ in figure 4b).

The CCD used to measure the IPRF in this study is a four-phase CCD. Everything discussed above is still valid for this type of CCD, the main difference being that each pixel is made up of four gates, and during integration two gates are held at high

voltages to collect charge instead of one, and the other two gates are held at a lower voltage acting as barriers just as with a 3-phase CCD.

# 4. SUB-PIXEL SENSITIVITY VARIATIONS AND IPRF MEASUREMENT TECHNIQUES

## 4.1 The Intra-pixel Response Function

The sub-pixel sensitivity variations observed in CCDs are described by the intra-pixel response function (IPRF), which maps the sub-pixel response as a function of illumination position at different wavelengths. Physical aspects of pixel structure can create non-uniform electric fields within a pixel causing sub-pixel sensitivity variations, and the diffusion of carriers tends to blur pixel boundaries, meaning the IPRF often extends beyond the pixel boarders.

As shown by Lauer,[19] the pixel response function (PRF) can be expressed in relation to the IPRF as

$$PRF = PSF * IPRF \tag{3}$$

where $PSF$ is the optical point spread function of the system and $*$ is the convolution symbol.

IPRF measurements have previously been performed for both front-illuminated[29–32,38,39] and thinned, back-illuminated[29,33–35,40,41] CCDs, as well as for CMOS detectors.[39,42–44] In general, the CCD studies have shown that the IPRF varies from detector to detector, with significant differences depending on the pixel structure and whether the device is front or back illuminated. It has also been shown that pixels tend to have the greatest response somewhere near their center, and the amount of light detected by the pixel near its edges is often about 50% less than the peak response. The IPRF has been shown to be spatially uniform;[29,41] that is, the IPRF does not vary significantly from pixel to pixel across the detector.

The shape and scale of the IPRF depend on the absorption depth in silicon of the incident light, and therefore the IPRF is both wavelength and temperature dependent. For a back-illuminated device, incident light that is absorbed deeper in the silicon is more likely to interact with the gate structure than light with a shorter absorption depth, which can greatly change the structure of the observed IPRF. For front illuminated devices, all light must pass through the CCD gate structure before being absorbed in the silicon. Therefore, the IPRF of front illuminated devices tend to show more structure at all wavelengths, while the IPRF of back illuminated devices has more structure at long wavelengths than at short wavelengths.

For situations in which the PSF is well sampled, the IPRF can be ignored. However, it is often the case that the PSF is undersampled and it has been shown that in these situations the IPRF can introduce significant error to the results of aperture photometry and astrometry,[19,32,34,35] as well as spectroscopy.[29] In these situations, knowledge of the IPRF can be used to correct this error and improve results.[19,45]

Also, as mentioned in section 2.2, the PSF is often not well known in situations of undersampling. If the IPRF of the detector is well measured, it can be deconvovled with the observed PRF of the system, and the optical PSF of the telescope can be determined. Knowledge of the optical PSF allows for the PSF fitting photometry technique to be used, which can be more precise than aperture photometry, especially for crowded fields.

## 4.2 Measurement Techniques and Results of Previous Studies

The first thorough study of the sub-pixel sensitivity variations of CCDs and the effects on undersampled images was performed by Jorden, Deltorn, and Oates in 1994.[29] They projected a demagnified pinhole of sub-pixel size onto a CCD and moved it in sub-pixel steps in single line scans across the horizontal and vertical directions, with an image taken at each spot location. They reported variations in the peak response of a single pixel on which the spot was incident of about 50% for both front and back-illuminated CCDs, and a change of signal within an aperture around the pixel of interest of up to 50% for the front-illuminated device measured, but only about 1-4% for the back-illuminated device measured. They also showed that intra-pixel response variations can have significant effects on undersampled spectroscopy.

Kavaldjiev & Ninkov[30–32] and Piterman & Ninkov[33–35] measured the IPRF of a front-illuminated and back-illuminated CCD respectively using a similar procedure as that described above, and obtained similar results. However, in testing the effects of the IPRF on undersampled data they focused on aperture photometry instead of spectroscopy, finding that in both cases a significant amount of error was introduced due to variations in sub-pixel response. Penny & Leese[45] reported that if the IPRF is known, corrections can successfully be applied to improve aperture photometry.

Other groups have studied the effects of sub-pixel response variations using dithered images of stars, not by directly measuring the IPRF. For example, it is known that both WFPC2 and NIC3 on the Hubble Space telescope undersample the optical PSF, more so with NIC3 than WFPC2. Holtzman *et al.*[46] used dithered images to determine that aperture photometry with WFPC2 varied by $\leq$2% depending on where

a star was centered on a pixel. Lauer[18,19] combined many dithered images to recreate a super-sampled PRF which he then used to create error maps that could be used to correct aperture photometry measurements. He found that for WFPC2, variations of ∼0.030 mag are observed, and for NIC3 the variation in aperture photometry can be a large as 0.39 mag. He then used his super sampled PRF to attempt to isolate the IRPF without direct measurement, essentially going about the task in the opposite direction of the other groups mentioned.

Both Jorden *et al.*[29] and Vorobiev *et al.*,[41] measured the IPRF directly and found that there was very little pixel-to pixel variation in the IPRF measurements of their CCDs.[29,41] However, measurements reported by Abdelsalam, Stanislas, and Coudert of a CCD with microlenses over the pixels found that although the signal detected at the edges of the pixels in each case is still about 50% of the maximum signal recorded, the shapes of the IPRF in the measured pixels show very significant pixel-to-pixel variations, which they attributed to inconsistencies in the shapes and thicknesses microlenses across the detector.[47–49] This indicates that when microlenses are present on the detector, it may be important to measure the IPRF of all pixels, whereas for CCDs without microlenses, the measurement of one pixel, or a few pixels spread across the detector to be safe, is sufficient.

Measurements of CMOS detectors reported by Mahato *et al.*[42,43] show IPRF variations similar to those found in previous CCD measurements. However, Ivory *et al.*[44] reported variation in the IPRF of $\leq 7\%$ for 470 nm and 624 nm light, and up to a 20% variation at 940 nm, much less than what has been reported for both front and back illuminated CCDs, as well as the other CMOS measurements mentioned here. Both used procedures similar to those described for the CCD measurements above and it is unclear why the values reported by Ivory *et al.* are so much lower than the others.

Methods other than the simple spot projection method above have also been developed. IPRF measurements are of interest for wide field near-infrared (NIR) missions as well as for visible light missions. The University of Michigan has devised a way to measure the IPRF of every pixel in a NIR detector in a reasonable amount of time (about 1 day) using the "Spots-O-Matic",[50] building off of its predecessor the "Spot-O-Matic".[51] As the names suggest, the Spot-O-Matic performed spot scans with a single spot, but the Spots-O-Matic uses an array of 160,000 spots spread out over the detector area to measure the IPRF of many pixels at one time. Aside from the spot projection, the method remains much the same as previous studies. However, to determine the

IPRF, the spot size used in the measurement must be well characterized. Because many spots are being used, each projected by its own pinhole and imaged by a different region of the lens used for demagnification, variations in spot size and shape are likely. Using this method, more time must be spent characterizing the the spots to ensure proper IPRF measurements across the array.

Another group used what they called the "ONERA technique",[52] in which they project periodic, high resolution patterns over the whole sensor using continuously self-imaging grating (CSIG) illuminated by plane wave. This pattern is moved across the detector so that one whole period of the pattern crosses each pixel. They then use a Fourier transform approach to determine the sub-pixel sensitivity variations across each pixel. Like the many-spot method, this method is faster than single spot scans of the entire detector.

The method adopted for the measurement of the IPRF in this study roughly follows the method described by Jorden *et al.*,[29] but some improvements to the procedure have been made. This is discussed in detail in section 5.1.

# 5. MEASUREMENT OF THE *KEPLER* CCD IPRF

As the number of wide field space based missions has increased, more missions have started including IPRF measurements in pre-flight preparation. For example, the IPRF has already been measured for the JWST detector,[53] and the ESA now requires IPRF measurements to be made for all detectors used in future space missions. The IPRF is also being considered more often in models of high-precision photometry[54] and radiometry.[55]

We have developed a method, described in this section, that has been used to measure the IPRF of a flight spare *Kepler* CCD, but that could be easily adapted to do the same for current or upcoming missions that also undersample the optical PSF of the telescope.

**The research presented in this section has already been published.[41]**

## 5.1 Experimental Setup and Spot Scan Procedure

To directly measure the *Kepler* CCD's IPRF, a spot scanning experiment was set up in a basement lab in the Carlson Center for Imaging Science. This lab has a separate foundation from the rest of the building which gives added stability to our setup. The method used here to measure the IPRF closely follows that of Jorden *et al.*;[29] however, more advanced technology was used to decrease error and increase the speed of the measurements. Images of the spot scan setup are shown in figures 6 and 7.

An Acton Research Corporation 0.5 meter monochromator with spectral bandwidth of $\Delta\lambda = 15$ nm was used to filter light produced by a broadband Energetiq EQ-99XFC laser driven light source. The light source produces a stable broadband spectrum over the full wavelength range at which we make our measurements. Scans were made for wavelengths of $\lambda = 400 - 850$ nm, every 50 nm with an additional set of scans at $\lambda = 425$ nm. The wavelengths used in the measurements were chosen to span the broad spectral bandpass of the *Kepler* mission. For scans at wavelengths longer than 700nm, a Bessel I filter was added to the optical path to remove any higher order light that might have been present.

The filtered light is projected onto our CCD using a 20X Mitutoyo Plan Apo NIR infinity corrected long working distance microscope objective. The objective works across the entire spectral band of interest, and focuses the light down to $\leq 3$ $\mu m$ depending on the wavelength (see section 5.2.1).

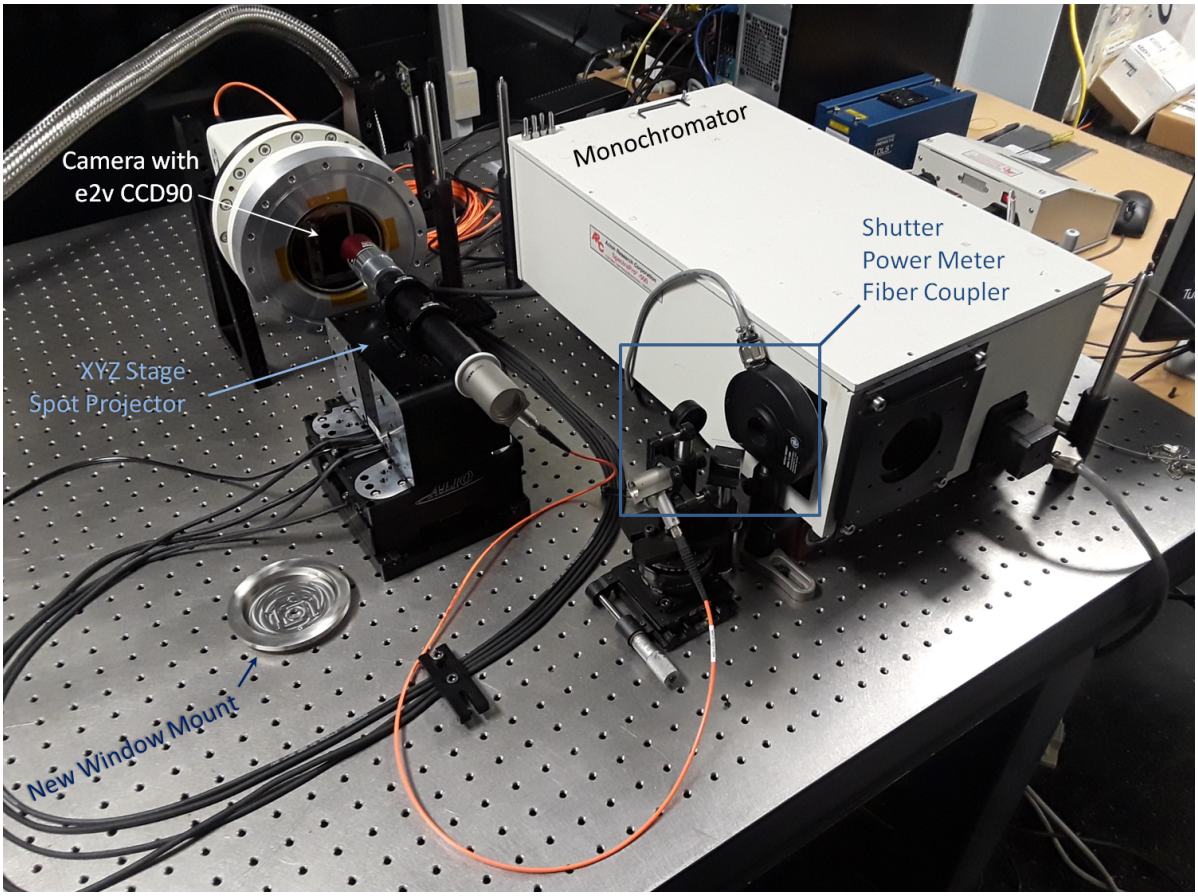


Figure 6: The spot scan apparatus used to measure the IPRF of the e2v CCD90.

The CCD for which we are measuring the IPRF is an e2v CCD90 (SN 208) flight-spare *Kepler* CCD. It was obtained through the NASA Ames Research Center, from the Ball Aerospace Corporation. The sensor is housed in a Spectral Instruments 800 Series camera. The original window was replaced with a fused silica window $500\mu m$ thick and 10mm in diameter, surrounded by a steel frame. Its small size reduces the amount of stray light that reaches the CCD while still allowing thousands of pixels to be accessible for measurements. The window was installed off-center and its location can be rotated to access even more pixels if necessary (figure 7).

The camera used in the lab is only capable of being cooled to -45°C, much warmer than the *Kepler* mission operating temperature of -85°C. This must be considered when interpreting our IPRF measurements because photon absorption depth in silicon is temperature dependent; therefore, we expect the IPRF that we directly measure will be slightly different than the IPRF at the *Kepler* operating temperature. This is discussed

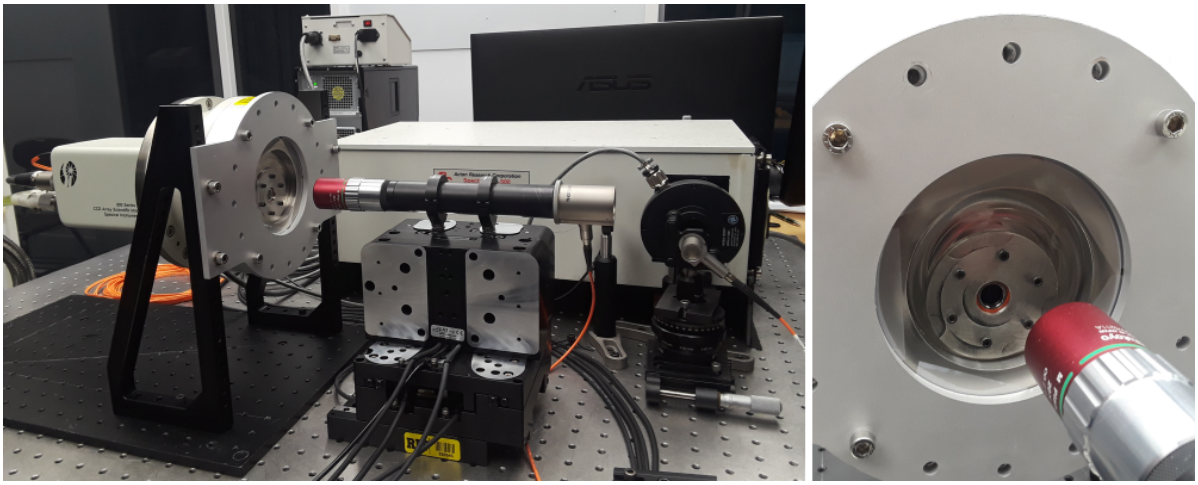

Figure 7: The same setup shown in figure 6, but the original camera window has been replaced with a smaller fused silica window surrounded by a stainless steel frame.

further in section 5.6.

The setup uses an XYZ translation stage from Alio Industries to move the spot instead of moving the camera itself. The minimum step size for the XYZ translation stage is 2 nm, with bidirectional repeatability equal to 20 nm. By choosing to translate the spot projector instead of the camera, the setup can be easily adapted to measure the IPRF of other detectors by simply switching out the camera. The translation stage and camera are both controlled by the same computer, which coordinates the stage movement and image capture, allowing for the automation of an entire scan. The length of a full scan depends on the exposure time chosen for the images as well as the size of the region being scanned and the step size used.

For each wavelength, three scans were performed one after another. A 54x54 $\mu m$ region of the CCD centered on a pixel of interest was scanned in 1 $\mu m$ steps with a subarray of the CCD read out at each spot location. For each scan, the spot was first stepped 54 times horizontally, then returned to the start of the row and stepped one step vertically, then across the horizontal direction again. This process was repeated until the whole region of interest was covered. Once a scan was completed, the spot was moved back to its starting location before a new scan began.

Because focal distance is wavelength dependent, the spot was refocused for each wavelength measured. To focus, the spot was located near the center of a pixel and stepped through a series of focus positions with an image taken at each. The location resulting in the peak brightness in the pixel of interest was used as the focal distance

for that wavelength.

## 5.2 Spot Size Determination

As shown in equation 3, the PRF observed in an image is the convolution of the optical PSF with the IPRF. This indicates that, unless the pixel is illuminated with an infinitesimally small point of light, which is not physically possible, what is measured using the spot scan method is not the IPRF, but the IPRF convolved with the optical PSF of the projected spot. Therefore, in order to isolate the IPRF, the shape and size of the optical PSF of the spot must be well known.

A previous study using the same experimental setup that was used here determined that the shape of the PSF is roughly circularly symmetric and has a full-width at half-maximum (FWHM) of about 4-5 $\mu m$ at the largest.[40] To get a more accurate measurement of the PSF of the spot, a Cannon 120MXS CMOS sensor with 2.2 $\mu m$ pixels was used to measure the spot. Although these pixels are much smaller than the pixels on the *Kepler* CCD, they are still too large to fully sample the optical PSF of the spot if its size is on the lower end of the expected range or smaller, so the spot size could not be reliably determined through direct imaging. Instead, the spot was slowly translated across ∼3 pixels centered on a pixel of interest in 0.1 $\mu m$ steps, with an image captured at each spot location to create a supersampled intensity profile. The spot size was expected to be wavelength dependent, so this process was repeated for each wavelength for which the IPRF was measured.

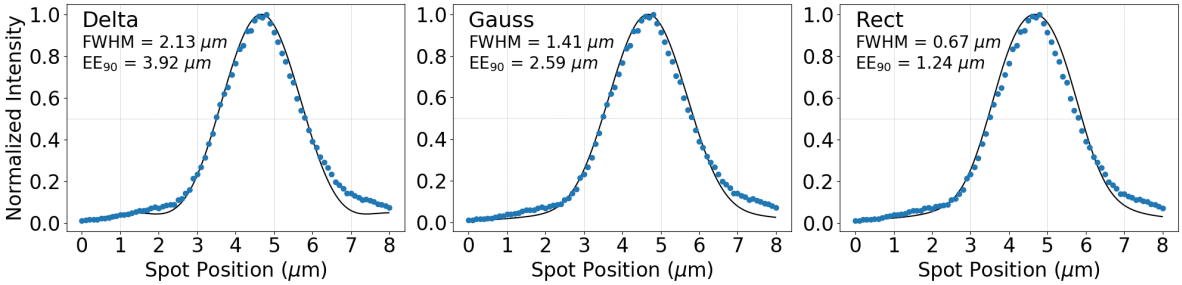


Figure 8: Example of the 3 different fits made to the PSF measurement at 700 nm, no window effects are included here. For each fit, the corresponding FWHM and 90% enclosed energy diameter ($EE_{90}$) are noted. Taken from Vorobiev et. al. 2019.[41]

To determine the size of the PSF of the spot, we must separate it from the IPRF of the CMOS sensor used in the measurement. Unfortunately, we do not know the IPRF of the Canon sensor with which we measured the PSF of the spot, so three possible IPRFs

were assumed. Assuming a uniform response across the whole pixel (Rect function) results in the smallest possible size for the corresponding PSF, while assuming a point, or delta, pixel response results in the largest possible size for the corresponding PSF. These IPRFs were used to determine the lower and upper bounds for the FWHM of our PSF respectively. The *most likely* FWHM of the spot was determined by assuming a Gaussian IPRF with 50% of the peak response at the edges of the pixel, which roughly agrees with previous IPRF measurements of CMOS detectors.[42,43]

To separate the PSF from the IPRF of the detector, a fit was made to the data using each of the three possible IPRFs listed above. The assumed IPRF, held at a fixed size and shape, was convolved with a spot, modeled as an Airy disk, whose width was allowed to vary. The size of the Airy disk that resulted in the best fit to the data for the given IPRF was recorded as the spot size. The fits for all three assumed IPRF shapes for the 700 nm measurement are shown in figure 8.

The FWHM of the spot for all wavelengths measured are shown as the dark dots in figure 9. In general, the spot size ranges from 1.25 to 2.50 $\mu$m, and is larger for shorter wavelengths. For wavelengths $\geq$ 700 nm, the spot size is diffraction limited.

### 5.2.1 Camera Window Effects on Spot Size

The *Kepler* CCD used to measure the IPRF has a small fused silica window that is 500 $\mu m$ thick located at the front of the camera housing. This window is expected to increase the spot size projected onto the CCD due to spherical aberration. To determine the effects of this window on the PSF of the spot, the spot size measurements were repeated following the same procedure outlined above at 3 wavelengths with a window identical to that of the CCD camera housing placed in front of the Cannon sensor. The window was carefully placed at the same distance from the Canon sensor as the window in front of the *Kepler* CCD.

As expected, the spot size measurements with the window in place were larger than those without. The results of the spot size measurement with and without the window in place are shown in figure 9. With the window in place, the reported spot size ranges from 2 to 3 $\mu m$ FWHM depending on wavelength and the assumed IPRF. The window and the choice of IPRF have a larger effect on the measured spot size in the infrared, than at shorter wavelengths.

It should also be noted that the Cannon sensor had its own window (of unknown thickness) located just in front of the detector. It is unclear exactly what effect this

has on the spot size measurement, but to be safe, we use the fit to the "with window" measurements as the spot size in our IPRF measurements, knowing that these measurements are most likely slightly larger than what is present on the CCD during IPRF measurements.

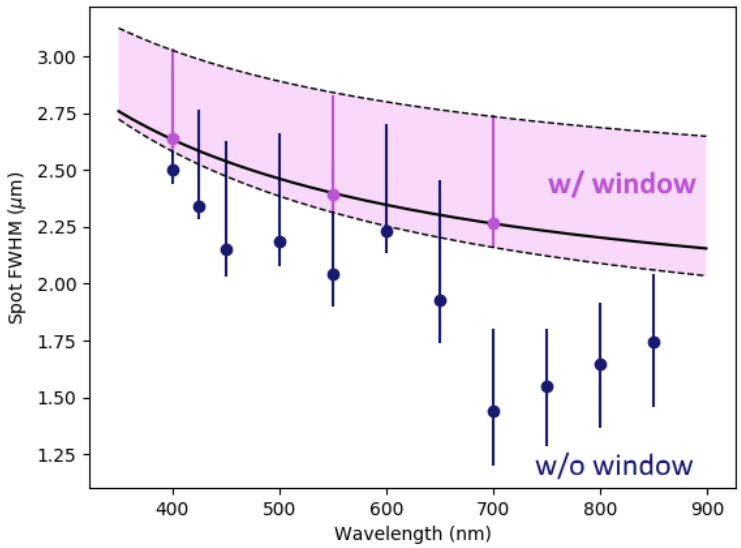


Figure 9: The size of the optical spot as measured for different wavelengths. The error bars show the upper and lower limits found by assuming a delta-like and a uniform IPRF respectively. The dark points show measurements made without the fused silica window in place, the lighter points are the measurements made with the window placed in front of the detector.

### 5.2.2 Effects of Spot Size on the Measured IPRF

One of the main effects that the IPRF attempts to characterize is diffusion of light incident on one pixel into neighboring pixels. However, because we are illuminating our pixels with a spot that has some physical size, at scan locations near the edges of a pixel, some light from the spot will be incident on the neighboring pixel and this effect will mimic diffusion in our IPRF measurements. To better understand this effect, we simulated spot scans for three different spot sizes assuming pixels with a perfectly uniform IPRF. In this case, any blurring observed is due to the physical size of the spot, not diffusion. Results of these simulations are shown in figure 10.

The first row of this figure maps the maximum pixel value recorded for all spot locations, each plot has been peak normalized. This is analogous to the probability

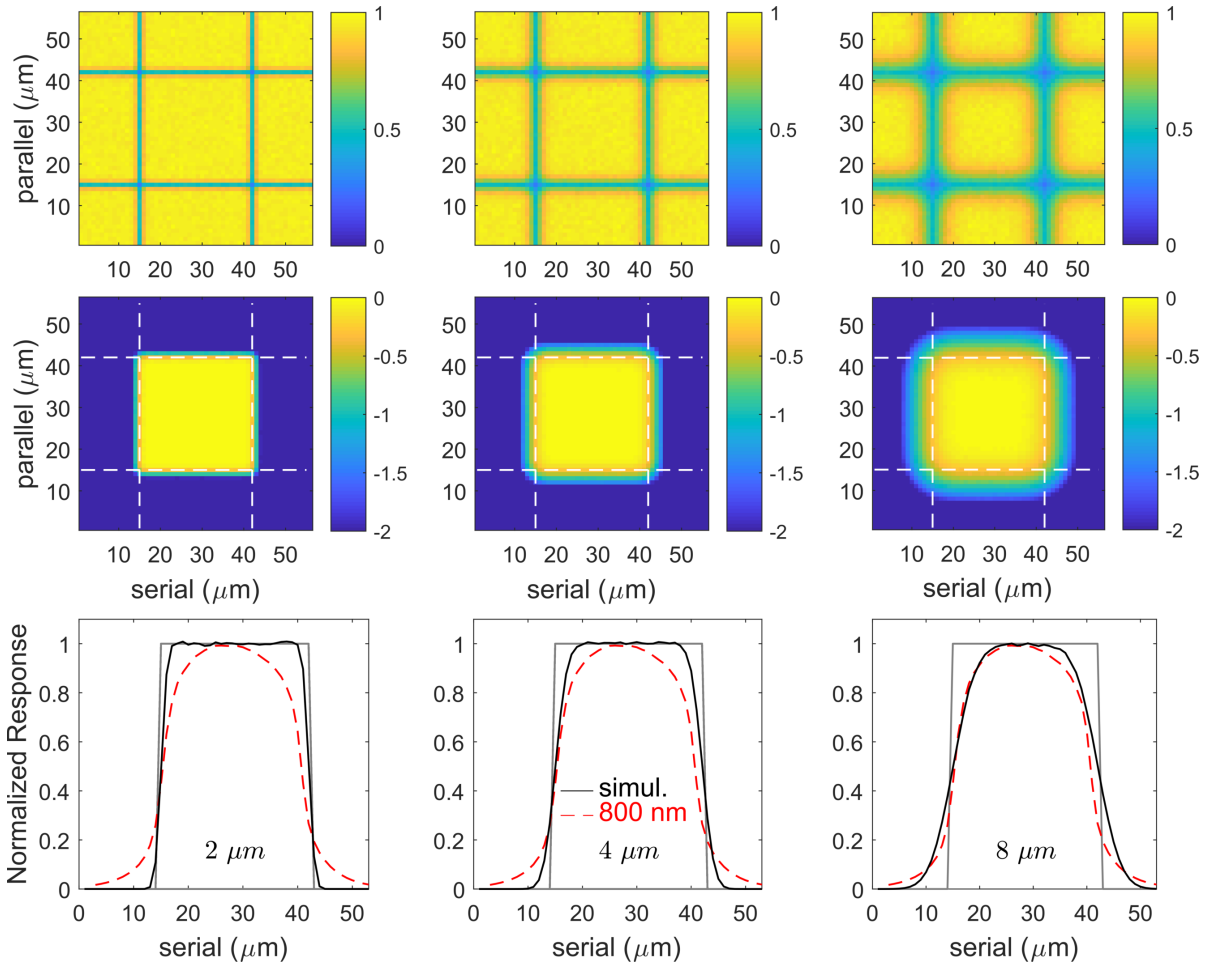


Figure 10: Results of spot scan simulations with different spot sizes and a uniform IPRF. The top row shows the peak-normalized raw output from a simulated scan. This is analogous to the "probability" that a photon is recorded in a particular pixel as a function of spot position. The middle row shows the response of a single pixel as a function of spot position. The bottom row shows a horizontal profile across the maps shown in the second row compared to the profile of our actual scan at 800 nm, as well as the perfect IPRF modeled here (gray line).

that a photon will be recorded in the pixel the spot is centered on as a function of spot position. The second row shows the response of the pixel of interest for all spot locations. It is evident that the pixel of interest still records some signal when the center of the spot is located over neighboring pixels, appearing to blur the pixel boundaries. This blurring effect is more pronounced for larger spot sizes.

The third row of this figure is the one we are most interested in. Here, the true pixel response is shown in gray, the simulated response as measured by the spot scan is

shown in black, and the actual response measured for our CCD at 800 nm is shown as the red dashed line. For the 2 $\mu m$ and 4 $\mu m$ spot sizes, the response measured with blurring solely due to the physical size of the spot (i.e. no diffusion) is easily distinguished from the measured response at 800 nm for which diffusion occurs. For an 8 $\mu m$ spot, the amount of blurring due to the spot size becomes indistinguishable from the blurring due to diffusion in the measured response shown. In this case, it would be very difficult to distinguish the effects due to the physical size of the spot from the effects due to diffusion.

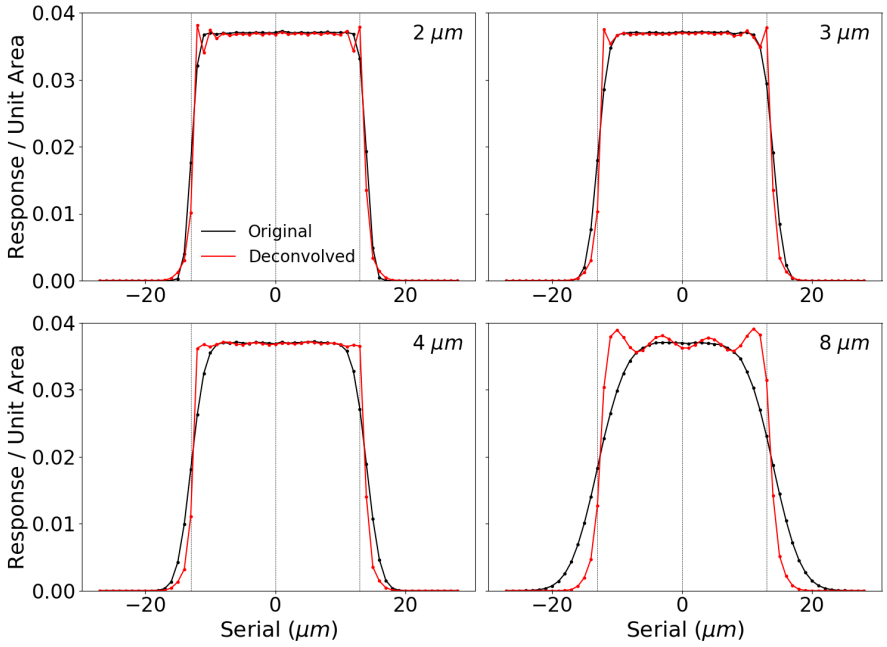


Figure 11: Results deconvolving the PSF from the measured pixel response to reconstruct the (known) IPRF. For the reconstruction of the IPRF using the 8 $\mu m$ spot, large errors are introduced.

Figure 11 shows the attempt to reconstruct the known IPRF by performing Lucy-Richardson deconvolution on the simulated response measurement and the spot for four different spot sizes. This plot confirms the observations made of figure 10 that up to a spot size of about 4 $\mu m$, the effects due to spot size can be separated from the effect due to the pixel response (i.e. the true IPRF is pretty well recovered using deconvolution). The pixel size used in these simulations was chosen to match that of the CCD used to measure our IPRF which has pixel pitch 27 $\mu m$, therefore a spot size of $\sim$1/6 the pixel size or smaller is required to accurately reconstruct the IPRF of the pixel.

## 5.3 Measurement Results

Raw measurements of the pixel response must be deconvovled from the PSF of the spot to determine the IPRF. Figure 12 shows profile plots along the parallel direction of the raw results as well as the deconvolved IPRF for all wavelengths measured. The edge plots show the profile of the volume normalized 2-D maps along the parallel direction. The "Original" data are shown with $2\sigma$ uncertainty shaded about the line. To be exact, using the three spot scans performed at each wavelength the bounds are calculated as: lower bound = median - $2\sigma$ and upper bound = median + $2\sigma$, where $\sigma$ is the standard deviation of the scans taken at that wavelength.

The spot size has a larger effect on the results of short wavelength scans than on long wavelength scans. The majority of photons at shorter wavelengths are absorbed within the first few microns of the silicon, farther from the gates, so we expect a significant amount of the blurring to be due to diffusion, and very little to be due to the physical size of the spot (as discussed in section 5.2.2); therefore, deconvolution of the spot should not have a large effect on the shape of the IPRF. For wavelengths $\geq$ 700 nm, the deconvolutuion has a greater effect on the resulting IPRF. The photons at these wavelengths travel further into the Si, and many are absorbed in the depleted region, making diffusion much less likely. Therefore we would expect the effects due to the spot size to be more significant as is seen in this figure.

For better comparison, edge plots of the deconvolved IPRF for three wavelengths in both the serial and parallel directions are shown in figure 13. These plots were created the same way as the edge plots described above. Because the IPRF is volume normalized the profiles can be directly compared to each other, unlike peak-normalized plots which can only be used for relative comparisons of IPRF shape.

For short wavelengths, the IPRF is smooth and shows Gaussian-like fall-off towards the edges. As the wavelength increases, the IPRF becomes flatter and the fall-off near the edge of the pixel is steeper. The more gradual fall-off observed for shorter wavelengths is the result if diffusion into neighboring pixels. As the wavelength increases, photons are more likely to be absorbed closer to the gates in the depletion region and less likely to diffuse, resulting in the more well-defined edges observed in the IPRF at long wavelengths.

Also at long wavelengths, effects due to the gate structure become visible. The gates that make up a pixel create varying electric fields along the parallel direction of

the device, and more uniform electric fields along the serial direction (the direction along which individual gates are laid). This causes the IPRF to show more variation along the parallel direction, and a more uniform profile in the serial direction in the 850 nm profiles shown in figure 13.

To highlight the wavelength dependence of the shape of the IPRF, peak-normalized 2-D contour plots are shown in figure 14. The extent of the IPRF into neighboring pixels is clearly shown here, indicating that the contribution of diffusion to the IPRF is more significant for shorter wavelengths, while the IPRF at longer wavelengths is more confined to the central pixel. Also, the IPRF at short wavelengths is almost circularly symmetric, while at longer wavelengths the shape is more square, and more structure is observed in the parallel direction than the serial direction as was seen in in the 850 nm profile plots. These results are similar to those observed in previous studies of other back-thinned CCDs.

While these individual IPRFs are useful in understanding the wavelength dependence of the IPRF, they cannot, on their own, be used to correct data from *Kepler* which is collected using a broad spectral band. Therefore, in order for these measurements to be useful, we must combine them to create an "effective" IPRF that can be applied to the data.

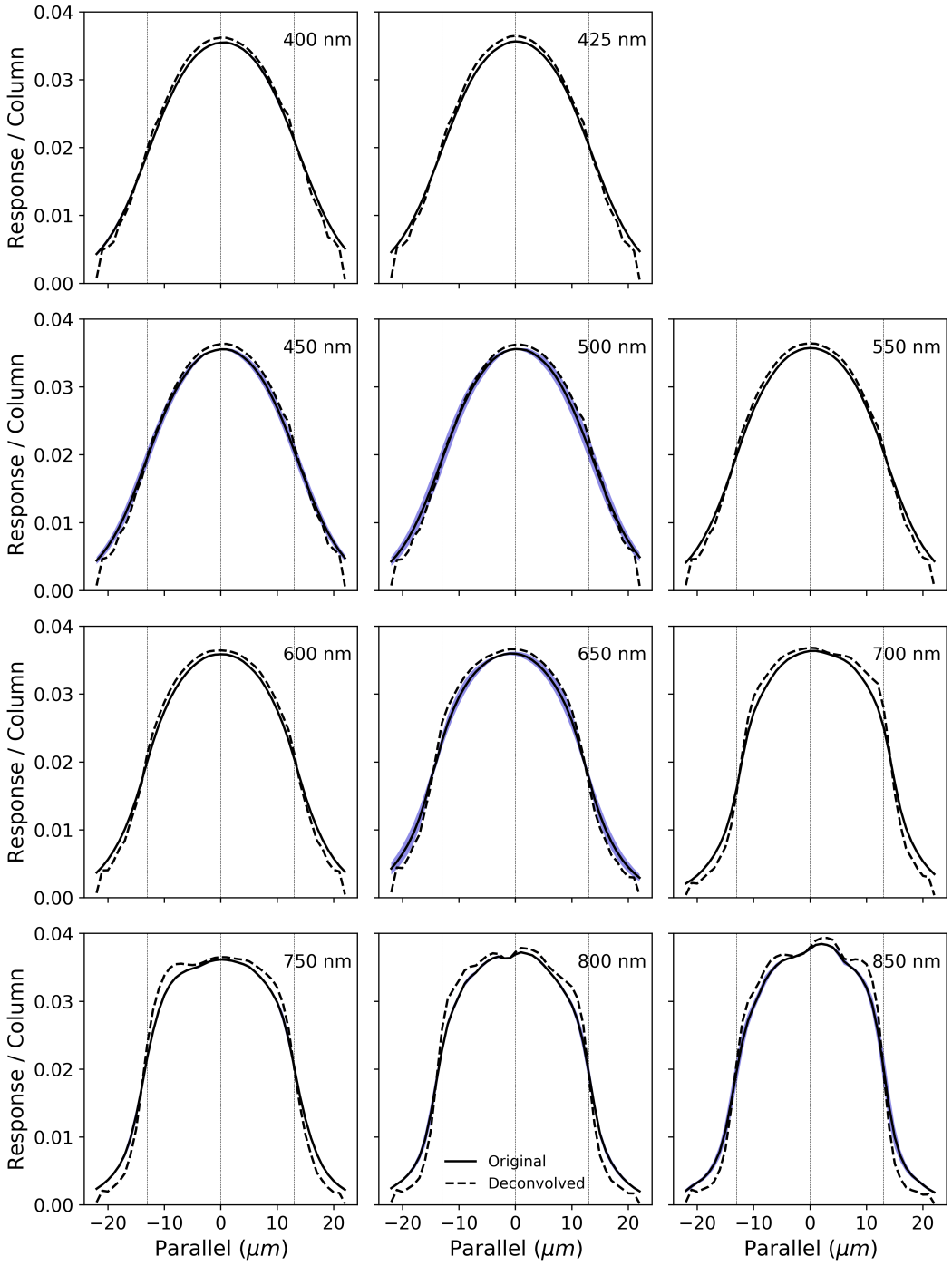


Figure 12: Profiles of the 2-D raw results (volume-normalized) are corrected using Lucy-Richardson deconvolution to separate the IPRF from the PSF of the optical spot.The original edge profiles are shown with the $2\sigma$ uncertainty range shaded around the line. For most scans, the uncertainty falls within the thickness of the line. Profiles created by volume normalizing the 2-D raw results or IPRF and summing along columns of the 2-D arrays.

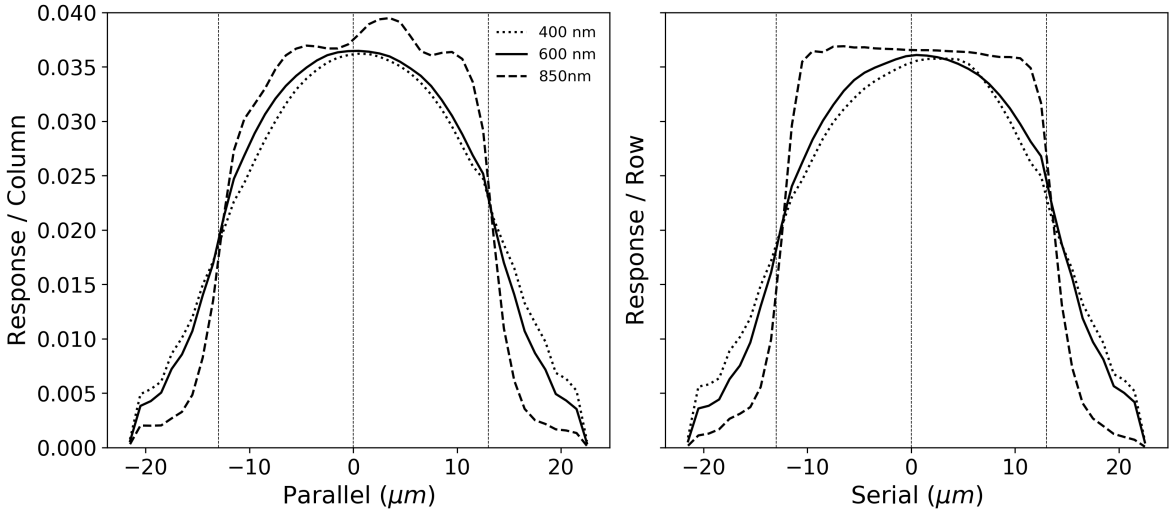


Figure 13: Profiles along the parallel and serial directions of the measured IPRF for three representative wavelengths shown as profiles based on the volume-normalized 2-D maps. Profiles created by volume normalizing the 2-D IPRF data array and summing along columns for the parallel profile and rows for the serial profile.

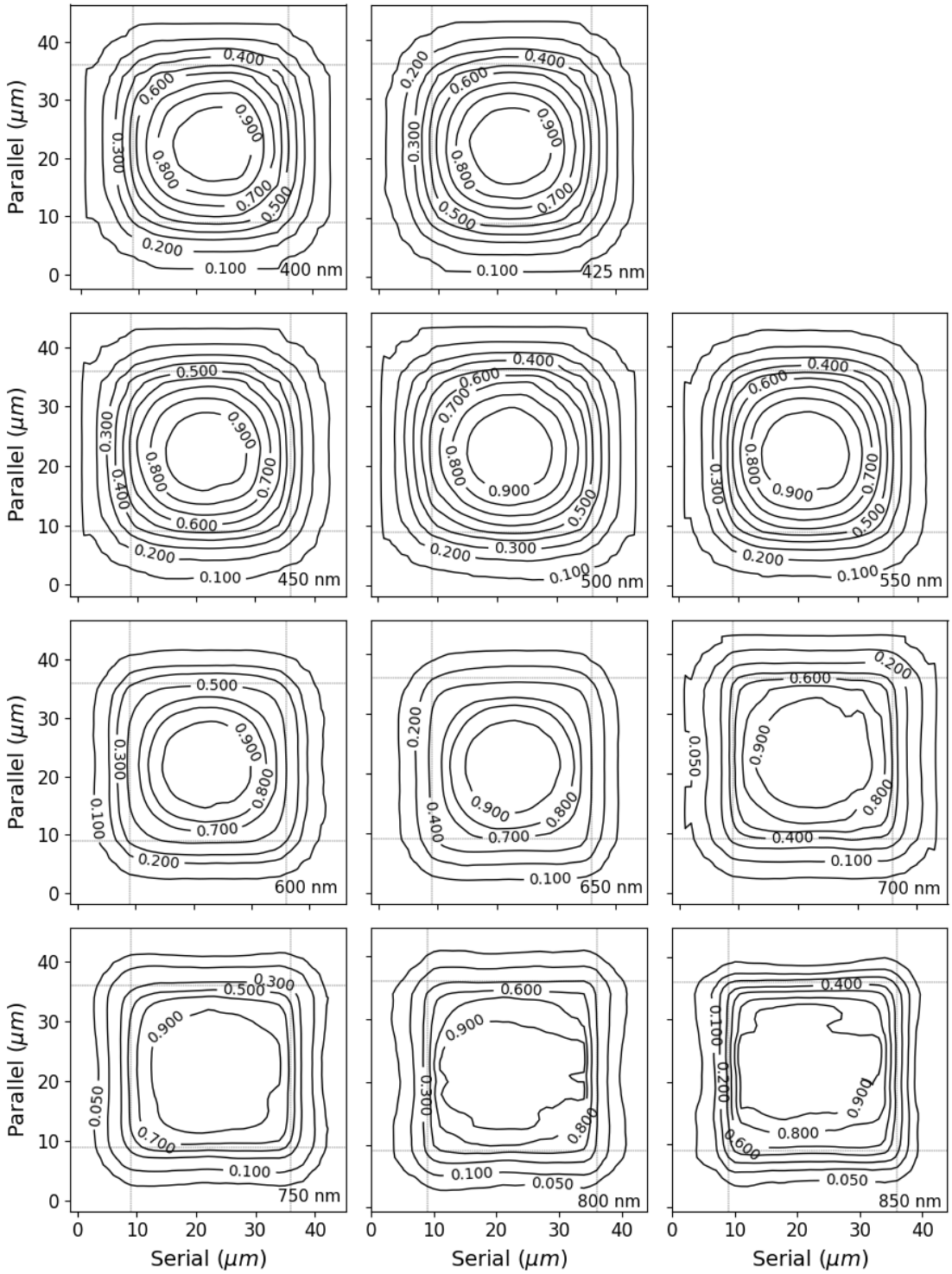


Figure 14: Contour plots of the IPRF at all measured wavelengths. Each map is peak-normalized to show the wavelength dependence of the IPRF shape.

## 5.4 The Effective IPRF

The individual IPRF measurements for wavelengths across the *Kepler* spectral band are only useful when combined into an "effective" IPRF, which depends on the spectrum of the object being observed, as well as the overall *Kepler* response. We suggest calculating this effective IPRF using a weighted average based on the stellar spectrum of the star that has been scaled by the *Kepler* response. The *Kepler* response and examples of stellar spectra of a G1V star and an M2V star are shown in figure 15a.

To obtain an effective IPRF, the stellar spectra are first scaled by the *Kepler* response. The peak normalized, scaled spectra are shown in figure 15b. The scaled spectra are then used to weight the IPRF measurements to create the effective IPRF.

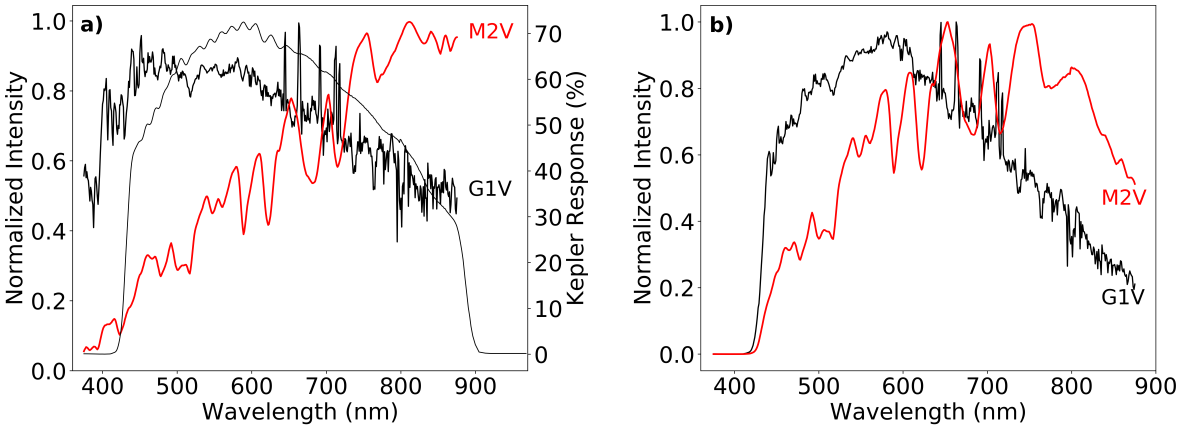


Figure 15: a) The peak normalized intensity of a G1V star and an M2V star, and the *Kepler* response curve (thin black line). b) The same two stellar spectra, this time scaled by the *Kepler* response curve. The scaled stellar spectra have been peak normalized after scaling.

For each wavelength at which the IPRF was measured, the area under the curve for a 50 nm section of the scaled spectrum of the star of interest, centered on the wavelength of interest, is summed. This value is used as the weight for the corresponding IPRF measurement in the weighted average. A comparison of edge plots of the effective IPRFs for an M star and G star, as well as the effective IPRF taking only the *Kepler* response into account, are shown in figure 16.

We expect that the slight differences in the shapes of the effective IPRFs shown in this plot will have an effect on aperture photometry once the response per unit aera shown is integrated over the entire pixel area. Although the significance of these effects is not yet known, using the appropriate effective IPRF for the stellar type of the star

being observed may allow for better corrections and result in slightly better photometric precision than using the effective IPRF calculated using only the *Kepler* response curve. This will be tested in future simulations of *Kepler* photometry.

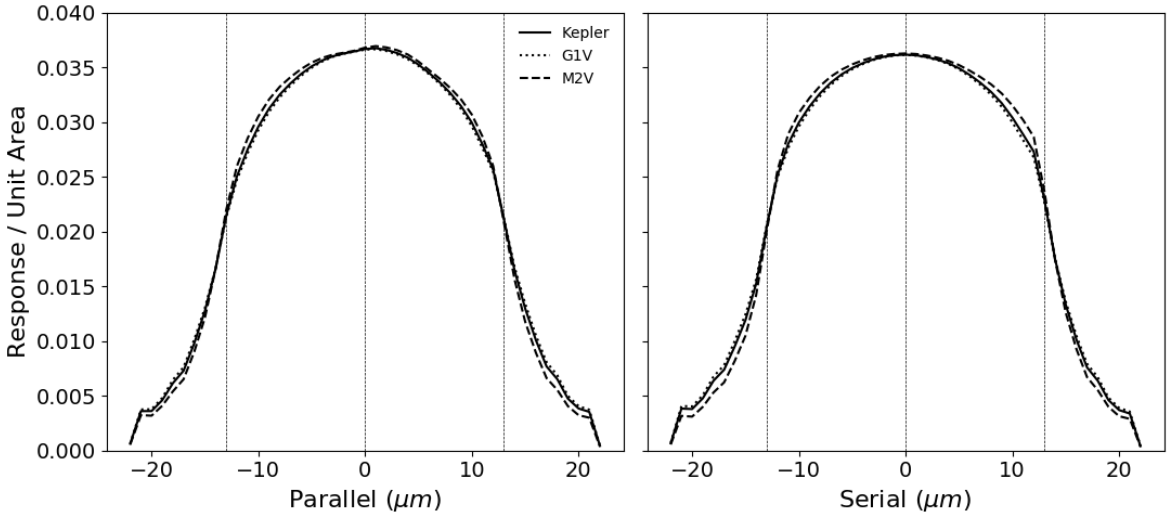


Figure 16: The "effective" IPRF for an M star and a G star compared to the weighted *Kepler* IPRF in the parallel and serial directions.

## 5.5 Spatial Uniformity

Pixel-to-pixel non-uniformity of the measured IPRF can arise due to non-uniformity in the fabrication process of a CCD. Factors such as the structure of the gate electrodes, thickness of the Silicon-oxide insulation layer, and doping uniformity in the epitaxial Si layers can affect the electric field structure within a pixel, which in turn can affect the IPRF of the pixel. Generally, scientific grade CCDs exhibit fantastic spatial uniformity, so we expect the spatial uniformity of the IPRF to be excellent as well.

A previous study reported that, as expected, the IPRF of a CCD does not change significantly from one pixel to another.[29] Therefore, for this experiment we measured the IPRF for a single pixel of interest for all wavelengths. However, for the sake of completeness, we show a comparison between the results found here and the results of a previous study using the same CCD, but a different pixel of interest.[40] Comparisons of the IPRFs of the two pixels measured at three different wavelengths are shown in figure 17.

The two pixels measured were 1.566 mm (about 58 pixels) apart on the detector, and their measured IPRFs show good agreement. The IPRF of the pixel from the

previous study (pixel b) is shown in blue with uncertainty ($2\sigma$ range), and the IPRFs measured in this experiment are shown as a black line. There is more uncertainty in the IPRF along the serial direction than the parallel direction. While there are some minor differences in the IPRF measured for the two pixels, they seem to agree well along both directions of the pixel. Because the fabrication process is the same for the CCD measured here and the CCDs used on the *Kepler Space Telescope*, and the IPRF appears to show good spatial uniformity across the CCD measured, the IPRF measured here should apply to the CCDs used in the *Kepler* mission as well.

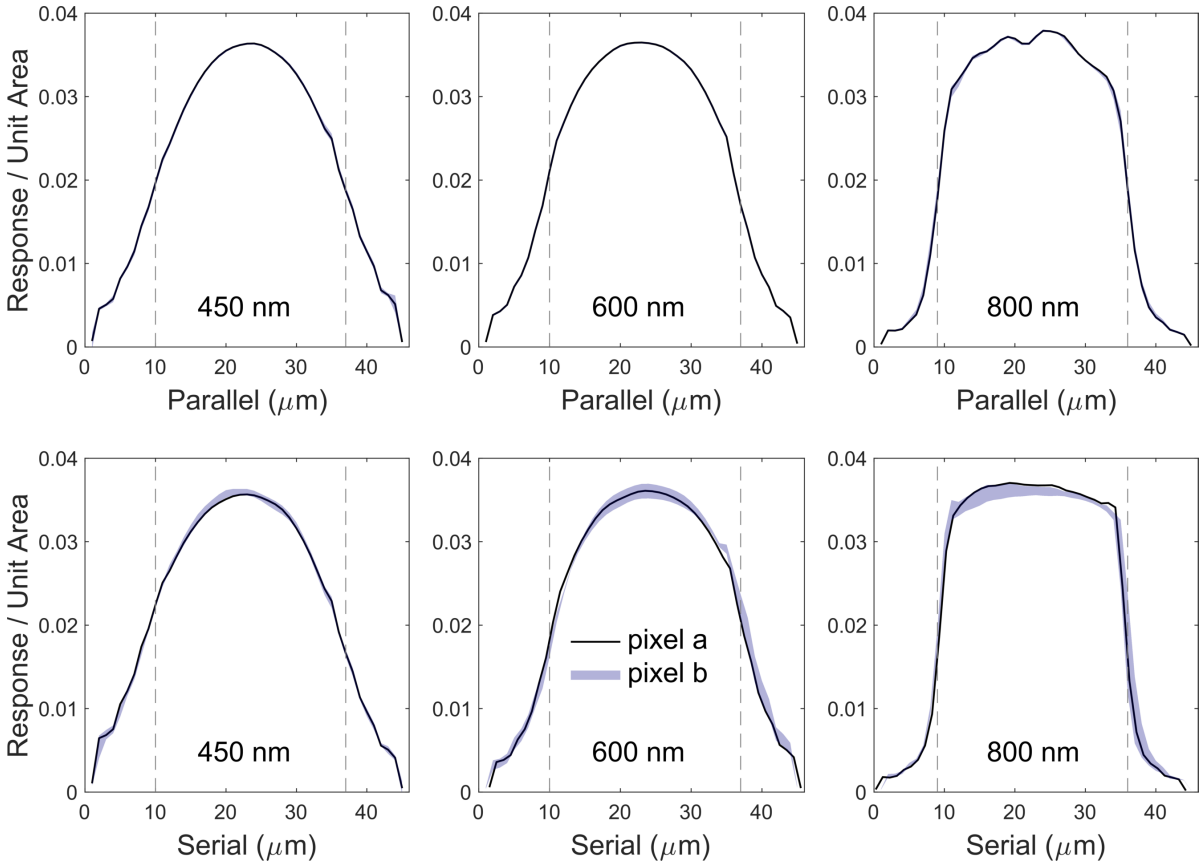


Figure 17: Edge plots along the parallel direction (top row) and serial direction (bottom row) for the current study (pixel a) and the previous study using a different pixel (pixel b). For pixel b, the measured IPRF is shown with the $2\sigma$ uncertainty defining the shaded region.

## 5.6 IPRF Temperature Dependence

The structure of the IPRF is highly dependent on pixel structure and the absorption depth in Si of the incident photons. We have shown that because the detector being

measured is a thinned, back-illuminated CCD, longer wavelength (red) light is absorbed deeper in the Si, closer to the gate structure, and exhibits more defined structure and less diffusion; while short wavelength (blue) light is absorbed farther from the gate structure and results in a smoother IPRF that extends further into neighboring pixels due to diffusion.

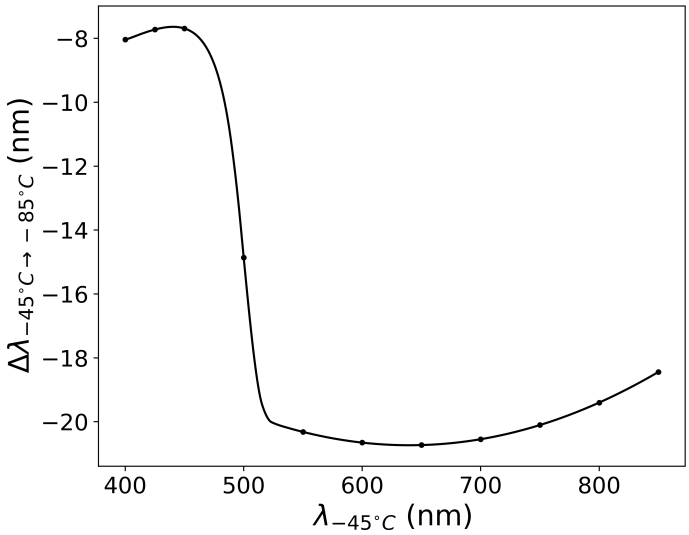


Figure 18: The change in absorption depth in Si from -45°C to -85°C.

However, absorption depth in Si changes not only with wavelength, but also with temperature as was discussed in section 3.2. The camera used to measure the IPRF of the *Kepler* CCD is only capable of being cooled to -45°C, while the CCD array aboard the *Kepler Space Telescope* is kept at an operating temperature of -85°C. Therefore our measured IPRFs cannot be applied to *Kepler* data without first considering the temperature dependence of the IPRF.

We explored this temperature dependence analytically using the model described by Rajnakan *et al.*[36] to calculate the absorption depth in Si at different temperatures. This model is applicable across our entire wavelength range of interest, and has been shown to be accurate for temperatures ranging from 20 to 500K. The absorption depths for temperatures of -85°C, -45°C, and +10°C are shown in figure 5. In general, the absorption depth increases as temperature decreases, but the change in absorption depth is larger for longer wavelengths.

To account for this change in absorption depth, we calculate the shift in wavelength that results in the same absorption depth in Si for -45°C and -85°C, the results of

this calculation are shown in figure 18. The IPRF measured in the lab at -45°C should be equivalent to the IPRF at -85°C that corresponds to this shifted wavelength. Since the absorption depth in Si increases as temperature decreases, the equivalent wavelengths are all shifted towards the blue with a median shift of 18 nm; which is comparable to our spectral resolution $\Delta\lambda = 15$ nm, and much smaller than the difference between wavelengths for which the IPRF was measured. Therefore, we believe changes in the effective IPRF will be minor for this change in temperature, so the effective IPRFs calculated here should also be applicable to *Kepler* data.

## 5.7 Focus and F-number Considerations

Further considerations as to whether or not we can directly apply our measured IPRF to *Kepler* data involve our method of focus and the f-number (f/#) of our system. Where we focus our spot within the Si has an effect on the spot size observed by our detector due to the absorption depth in Si at different wavelengths, as well as the f/# of the microscope objective used to create the spot. Because we are using a fast beam (f/1.146), the light diverges quickly before and after the focus, and where the spot is focused affects the *observed* spot size (as opposed to the spot size at the beam waist). If we do not take this into account, we may attribute "diffusion" to our IPRF that is actually divergence in the beam. This is dependent on the optics of the system being used and not an inherent property of the detector that we are trying to measure.

For a spot focused on the surface of the Si, the observed spot size will be different depending on the illuminating wavelength, even if the size of the beam waist remains the same. For the shortest wavelengths used, most of the photons will be absorbed within the first 0.5 $\mu$m of the Si, very close to the focus (figure 19a). In this case, ignoring diffusion, the observed spot size will be almost the same as the size of the beam waist. For longer wavelengths, photons are absorbed deeper in the Si (figure 19b) and diverge farther from focus before being absorbed. Because of this divergence the observed spot size will be significantly larger than the size of the beam waist. In this case, using a measurement of the beam waist as the spot size would result in some of the spread caused by the divergence of the beam to be attributed to diffusion in the IPRF. Therefore, the observed spot size for each wavelength must be measured and used to determine the IPRF, not the size of the beam waist. This is achieved using the spot size measurement technique described in section 5.2.1.

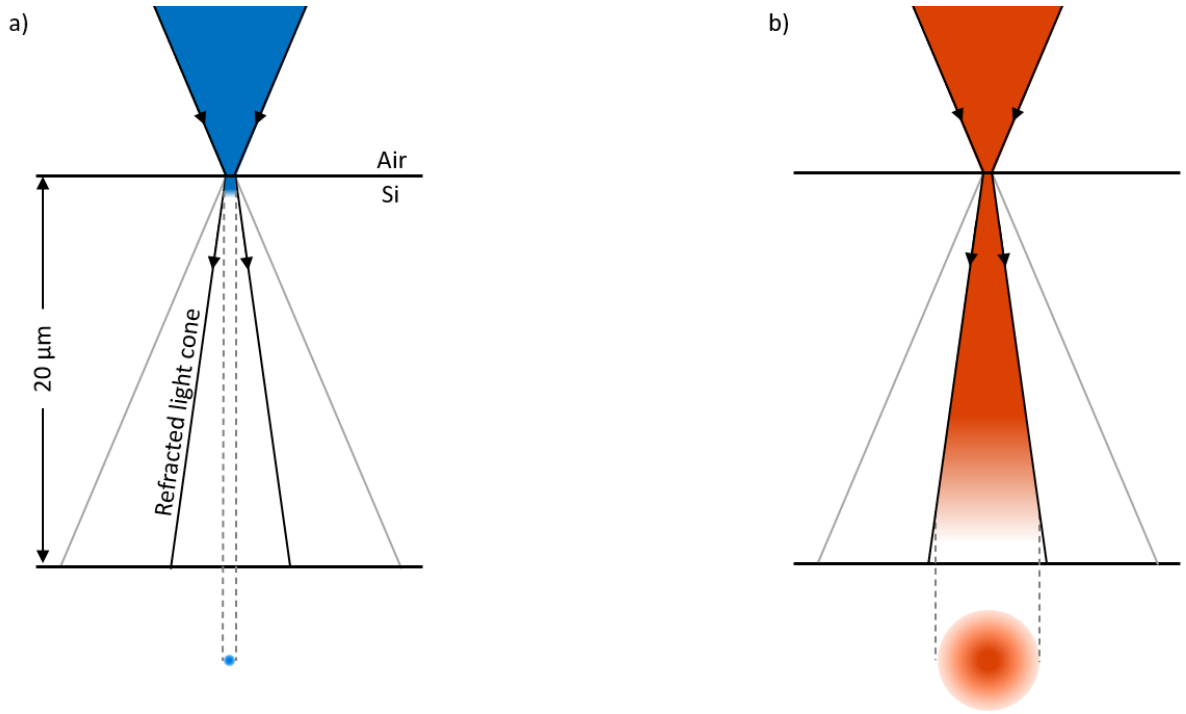


Figure 19: How the observed spot size is affected by the absorption depth in Si of the illuminating light. In both cases shown the beam is focused at the surface of the Si and the shaded gradient shows how far photons penetrate the Si. The resulting *observed* spot size in each case is shown at the bottom of the figure. a) Short wavelength light will be absorbed very close to the surface of the Si. Therefore, ignoring diffusion, the observed spot size will be very close to the size of the beam waist. b) For longer wavelength light, photons are absorbed deeper in the Si, resulting in an observed spot size that is larger than the beam waist.

Furthermore, to achieve the smallest observed spot size possible for each wavelength, and therefore the most reliable IPRF measurement, the beam must be focused at different depths within the Si depending on the wavelength of light being used. For a spot of long wavelength light focused on the surface of the detector, all photons absorbed in the Si diverge from focus resulting in a large observed spot size. By focusing the beam at some point within the Si, the divergence from the focus can be minimized; however to determine this point, the absorption depth of the wavelength of light being used must also be taken into account.

Following O'Connor *et al.*,[56] the expected shift in objective position away from the position corresponding to focusing at the surface of the sensor can be found using the following two equations. First, to calculate the size of the beam at any point $z$ below the surface of the sensor for a given shift $\delta$,

$$\sigma(\delta, z) = \begin{cases} \sigma_w + \frac{|z - n\delta|}{2nf} & \delta > 0 \\ \sigma_w + \frac{|\delta|}{2f} + \frac{z}{2nf} & \delta < 0 \end{cases}, \tag{4}$$

where $\sigma_w$ is the spot size at the beam waist, $z$ is the distance below the sensor surface, $n$ is the index of refraction, $f$ is the f/# of the microscope objective or telescope, and $\delta$ is the shift in objective position away from the position corresponding to focusing at the surface. Here, $\delta > 0$ is a shift towards the detector resulting in focus occurring below the surface of the detector, and $\delta < 0$ is a shift away from the detector, resulting in focus occurring before surface of the detector. Then, to determine the observed spot size,

$$\sigma_{div}^2(\delta) = \frac{\int_0^d \sigma^2(\delta, z) e^{\frac{-z}{l_{abs}}}\, dz}{\int_0^d e^{\frac{-z}{l_{abs}}}\, dz}, \tag{5}$$

where $d$ is the detector thickness, in this case $d \sim 20\mu$m, and $l_{abs}$ is the absorption depth in Si for the wavelength of light illuminating the sensor.

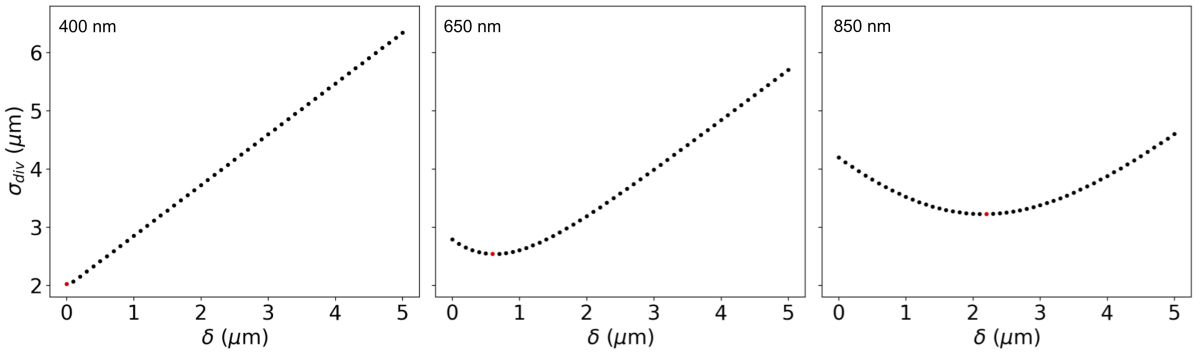


Figure 20: $\sigma_{div}$ as a function of  for $\lambda = 400$ nm, $\lambda = 650$ nm, and $\lambda = 850$ nm. The point corresponding to the smallest spot size and, therefore, the ideal objective shift is shown as a red point for each wavelength shown. For these calculations $\sigma_w = 2$ $\mu$m, which may or may not accurately represent the spot size at the waist of the beam used in this experiment. Changing $\sigma_w$ does not change the ideal shift.

For each wavelength, $\sigma_{div}$ was calculated for a range of objective position shifts (all positive) to determine the shift required to obtain the smallest *observed* spot size possible. The results for three wavelengths are shown in figure 20, and the expected shifts for all wavelengths are shown in figure 21(a). Once $\delta$ is known, it is possible to determine the ideal depth at which the beam comes to focus for each wavelength using

Snell's Law and geometry. The ideal focus depths, or the focus depth corresponding to the smallest observed spot size, for all wavelengths are shown in figure 21(b). For the shortest wavelengths the ideal focus, occurs at the surface of the detector, and the depth of the focus increases as wavelength increases.

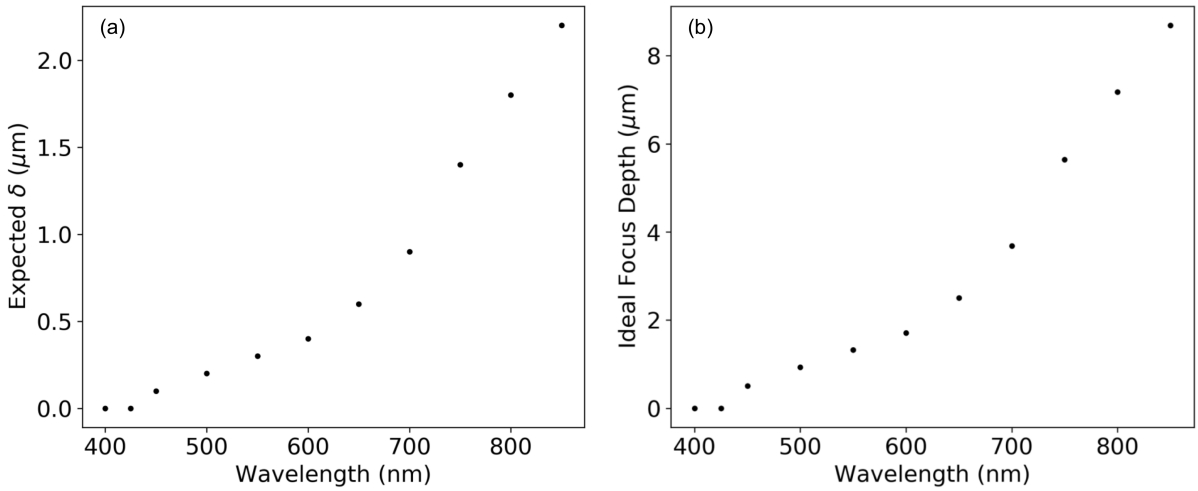


Figure 21: (a) The expected shift in objective position from the position corresponding to focus at the Si surface. (b) The position of the focus below the Si surface that results in the minimum observed spot size.

In this experiment, to focus the spot on the detector at each wavelength, a method was used that maximizes the amount of light detected in a single pixel (see section 5.1). Using this method, the spot is focused at the point within the Si for which the *observed* spot size is minimized. Therefore, we should be focusing near the locations of ideal focus shown in figure 21(b). This method was used for both the spot size measurement and the IPRF measurements.

By using this focus method we minimize the observed spot size, and the spot size measurement technique described in section 5.2.1 measures the observed spot size created by our beam, not the size of the beam wait. Therefore, our IPRF should not contain effects that are dependent on the divergence of the beam due to the f/# of the system used to make the measurement. Because of this, the measured IPRF should be able to be directly applied to *Kepler* data without any corrections to account for effects caused by the f/# of the system.

### 5.7.1 Chromatic Aberration in the Microscope Objective

The microscope objective used to form the spot is a Plan Apochromat objective, meaning it has been corrected to maintain very close to the same focal length across a specific

wavelength range (480-1800 nm). By comparing the results of the calculations shown in section 5.7 to the actual objective shifts required to focus in this experiment, we find that the focal length of the microscope objective does change with wavelength.

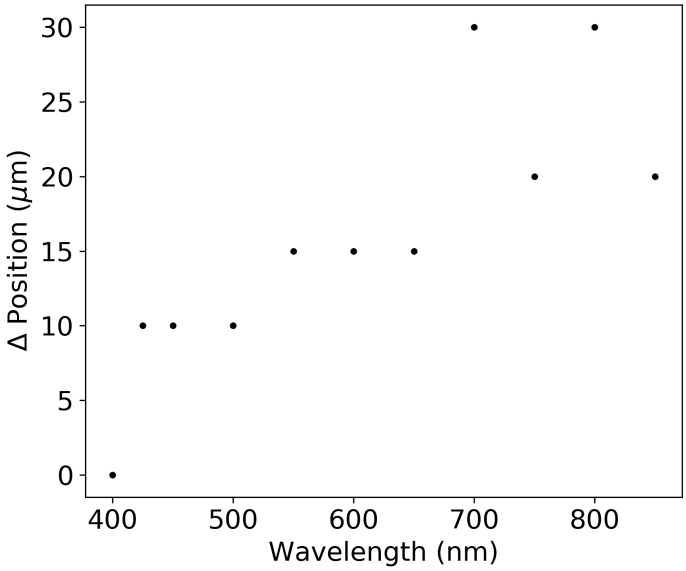


Figure 22: Objective position at ideal focus for all wavelengths used. For all wavelengths greater than 400 nm the shift is larger than would be expected given the ideal shifts shown in figure 21(a). All shifts shown are towards the detector.

For the 400 nm measurements, the spot is focused at the surface of the detector. If the focal length of the objective is exactly the same for all wavelengths used, the shift in objective position from the 400 nm position required to focus the spot at other wavelengths should exactly match the ideal shifts shown in figure 21(a). However, we observe larger shifts than expected for all wavelengths greater than 400 nm. The changes in objective position required to focus the spot for all wavelengths are shown in figure 22, positive shifts are towards the detector.

The change in focal length can be calculated by subtracting the actual shift in objective position from the expected shift, assuming we are focusing at the exact depth shown in figure 21(b) for all wavelengths. The results of this calculation are shown in figure 23. In general, the focal length tends to decrease as wavelength increases, and the magnitude of the largest change in focal length is 29.1 $\mu$m, or 0.29%. The step-like appearance of the data is caused by the large step sizes used to focus the spot in this experiment. For a more accurate measurement of the change in focal length, this would need to be repeated with smaller step sizes used in the focusing technique.

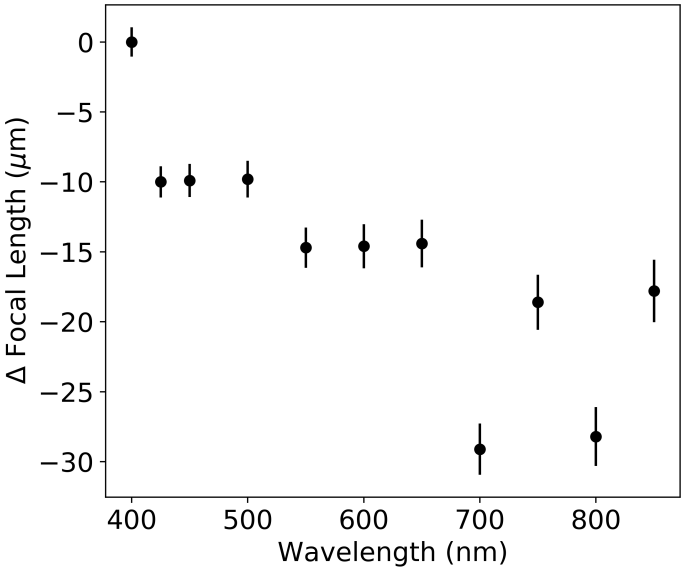


Figure 23: The change in focal length of the microscope objective from the focal length at 400 nm assuming we are focusing at exactly the absorption depth calculated in figure 5 for -45°C. The uncertainty given is the depth of focus of the beam at each wavelength.

# 6. SUB-PIXEL QE VARIATIONS

Ideally, every photon incident on a CCD will produce a photoelectron, and every photoelectron produced will be collected and counted. This is never the case though, and the ratio of the number of photoelectrons generated to the number of incident photons is called the quantum efficiency (QE) of the detector:

$$QE = \frac{n_{ph}}{n_{pe}}, \tag{6}$$

where $n_{ph}$ is the number of incident photons, and $n_{pe}$ is the number of photoelectrons.

Measuring the signal in a single pixel of interests in our spot scan images leads to a measurement of the IPRF as discussed in section 5. If we instead analyze the signal within an aperture surrounding our pixel of interest, we observe sub-pixel variations in QE. This section discusses the aperture photometry performed on our spot scan images, and the resulting sub-pixel QE variations measured.

## 6.1 Aperture Photometry of Spot Scan Images

Aperture photometry was performed on individual spot scan images for all scans at all wavelengths measured following the method described in section 2.1. Curve of growth analysis and SNR curves indicated that a 3x3 square aperture was ideal for these measurements. For stellar aperture photometry, it is common for a significant percent of the light to fall outside of the selected aperture. Here we have an isolated PSF that is much smaller than an individual pixel, and it was found that $\geq$95% of the total energy was contained within this 3x3 region for all spot locations and wavelengths. Therefore, changes in the flux within the aperture should be caused by actual variations in sub-pixel QE, not by light falling outside of the aperture due to spot location.

While trying to determine the ideal aperture size, it was found that the images did not have a uniform background, which was causing issues with the background annulus calculations. To deal with this, a background image was constructed by averaging all images in a scan, removing the region surrounding the pixel of interest so no light from the spot was included, and applying a fit to the region removed based the surrounding pixels. This background image was subtracted from each individual image in the scan, resulting in a much more uniform background, and better aperture photometry measurements.

After background subtraction, aperture photometry was performed on each individual image for each scan at each wavelength. The aperture was allowed to move to be centered on whichever pixel the spot was incident on in order to keep ≥95% of the light within the aperture for each image. The results for all three scans at each wavelength were averaged to give the final result. The variations in sub-pixel QE across a single pixel for three wavelengths are shown in figure 24. The values in each panel of figure 24 have had their mean set as the zero value, and the values in the color bar show percent changes in signal within the aperture.

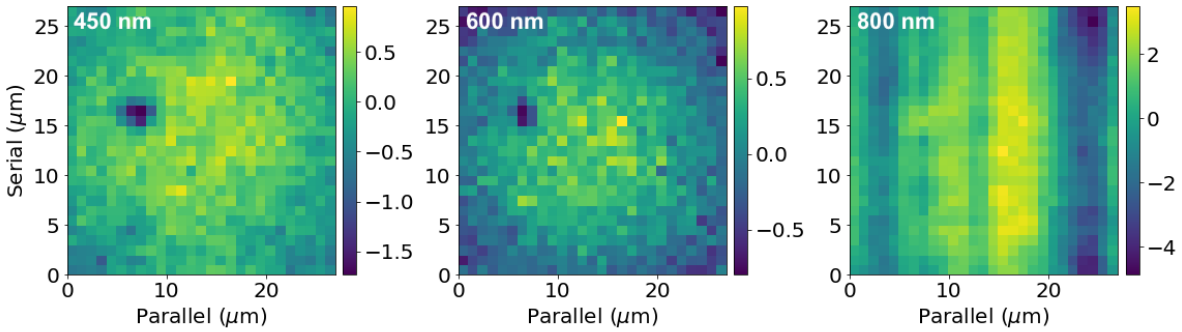


Figure 24: Sub-pixel QE variations for three wavelengths of light. The zero value shown is set to the mean value of the array, the scale shows percent variations in QE.

## 6.2 Discussion of Results

Analysis of spot scan images using aperture photometry revealed sub-pixel QE variations for all wavelengths analyzed. Like the IRPF, the sub-pixel variations in QE are wavelength dependent. The sub-pixel QE variations are more uniform for shorter wavelengths, and show more structure at longer wavelengths. The QE is observed to vary by up to 7% at the longest wavelengths, while the smallest variations of ∼2% are observed in the middle of the wavelength range measured, and the shortest wavelengths show variations between these values.

At long wavelengths, the pattern observed matches well with the known pixel structure of the CCD used in our measurements. The e2v CCD90 is a 4-phase CCD, meaning each pixel is made up of 4 gates along the parallel direction. In the 800 nm plot in figure 24, four distinct columns are observed (dark, bright, bright, dark) that line up with where we would expect the gate structures to be located within the pixel.

Also of interest is the spot on the left side of each of the plots shown in figure 24 that is darker than the surrounding are in the 450 nm and 600 nm plots, and brighter

than the surrounding area in the 800 nm plot. This is most likely a grain of dust located over the pixel that is absorbing photons at short wavelengths and causing interference effects at long wavelengths. We do not attribute the values in this area to actual sub-pixel QE variations.

The exact mechanism, or mechanisms, responsible for the QE loss at certain pixel locations is unknown. However, we think it is likely that the structure observed at long wavelengths is at least partially due to reflections off of the gates. As is shown in figure 4b for back-illuminated CCDs, short wavelength photons are unlikely to reach the gate structure of the CCD, resulting in a more uniform QE map, but it is likely that a decent number of long wavelength photons will make it all the way through the silicon. Depending on where they strike the gate structure, some photons may be more likely to be reflected back into the silicon than others and have a second chance to generate charge and be collected. If this is the case, we would expect the areas with higher QE values to be locations for which the gate structure exhibits higher reflectivity.

Along with the IPRF, the observed sub-pixel QE variations may have a non-negligible effect on aperture photometry. The simulated aperture photometry discussed in section 7 does not yet take the measured sub-pixel QE variations into account, but it will be included in future studies.

# 7. SIMULATED APERTURE PHOTOMETRY

Now that the IRPF has been measured, we are interested in how the presence of sub-pixel sensitivity variations affects the photometric precision of aperture photometry. To analyze this, we have created a model that could be easily adapted to study the effects of different IPRFs, as well as the one measured here.

For now, the aperture photometry simulation is kept very simple and general, taking into account only spacecraft jitter, drift, the measured IPRF, shot noise, and read noise. Later, more robust simulations of *Kepler* aperture photometry will be created to better understand the effects caused by the measured IPRF in this specific case and to test methods for correcting error introduced by the IPRF, as well as to attempt to extract a precise optical PSF using knowledge of the *Kepler* PRF and IPRF.

Because we are using the IPRF as measured on the *Kepler* CCD, some of the parameters for the simulation are selected to match those of the *Kepler* mission, *but much has been simplified and we focus on how the noise sources studied affect photometric precision in general.*

## 7.1 Simulated Observations

To study the effects of the measured IPRF on aperture photometry, as well as the effects of spacecraft jitter and drift, observations were simulated for stars across a range of magnitudes. All stellar magnitudes in this section are given in terms of their *Kepler* magnitude (Kp). The flux observed at the detector for a given *Kepler* magnitude is given by the equation

$$f_{kep} = 10^{-0.4(Kp-12)} \cdot f_{12}, \tag{7}$$

where $f_{kep}$ is the flux detected by *Kepler* in $e^-/s$, $Kp$ is the *Kepler* magnitude, and $f_{12} = 1.74 \times 10^5 e^-/s$ is the flux of a G2V star with $Kp = 12$.[21] We model observations across the magnitude range 12.0 to 16.5 Kp in half magnitude increments. For each magnitude, ∼3500 six second CCD integrations were simulated, which corresponds to about 6.5 hours of *Kepler* data. Each simulated image is 35x35 pixels in size and contains only one star, but background signal and various noise sources are included.

### 7.1.1 The Model PSF

For each simulated image, a super-sampled stellar PSF is created (figure 25) to match two main features of the *Kepler* PSF: 50% enclosed energy within the central pixel when

the PSF is centered on the pixel and a 95% enclosed energy diameter of ∼4 pixels,[9,20,21] this resulted in a PSF with a full-width at half-maximum (FWHM) of ∼1 pixel. The PSF is known to vary across the *Kepler* CCD array, so the parameters were chosen to represent features of the average PSF shape. The *Kepler* PSF is also known to be wavelength dependent and asymmetric with high spatial frequency features. We have not tried to recreate these features and instead adopt a simplified version created by summing two circularly symmetric Gaussians. Although we chose to match certain features of the *Kepler* PSF, this level of undersampling is typical of many wide-field surveys.[24,57,58]

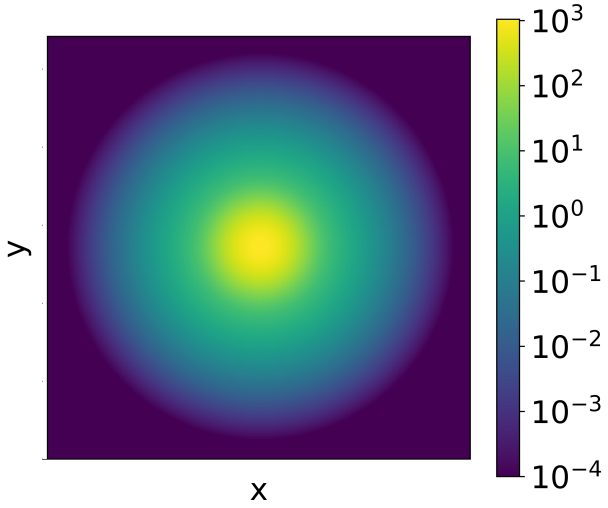


Figure 25: The super-sampled PSF corresponding to an 11x11 pixel region of the simulated array.

In order to appropriately convolve our PSF with the measured IPRF, the PSF must be defined at the same resolution as our IPRF. The IPRF was measured in 1 $\mu$m steps across the 27 $\mu$m pixels, so the same was done for our super-sampled PSF. For each magnitude, the PSF is scaled using equation 7 to give the appropriate flux. The PSF and the effective IPRF for a G star are then convolved. Before convolution, the IPRF is volume normalized so that the overall flux across the entire PSF remains the same. After the convolution, the array is binned into pixels by summing 27x27 regions of the array as shown in figure 26a.

Shot noise from both the source and background signal as well as read noise are then applied to this array. Here we use the median read noise reported for *Kepler*, which is 86 $e^-$/pixel.[21] This is the final image on which the aperture photometry will be performed.

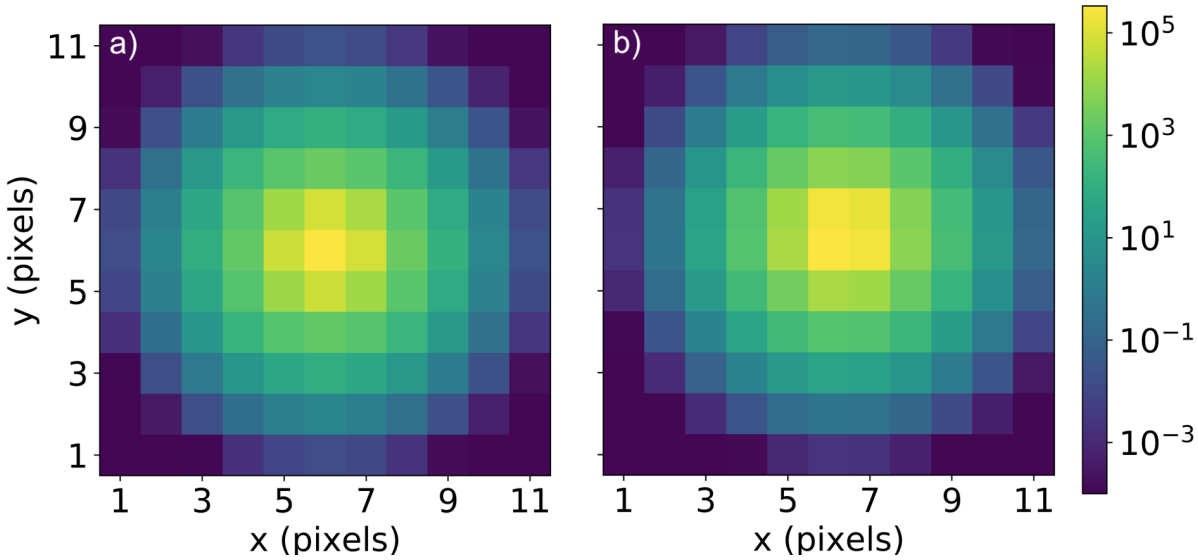


Figure 26: a) The same PSF shown in figure 25 binned into pixels. The PSF of this star is centered on a pixel. b) The binned PSF of a star centered near the corner of a pixel.

### 7.1.2 Modeling Spacecraft Jitter and Drift

To model spacecraft jitter, for each image the PSF position is randomly selected from a Gaussian distribution centered on a specified region of a pixel. The selected position is used as the location of the center of the PSF of the star for that image. Jitter distributions with standard deviations of 0.03 pixels and 0.06 pixels were modeled. These jitter values are larger than the values reported for *Kepler*,[9,59] but are typical for other missions with lower pointing stability such as CubeSat missions.[60] The purpose here is to show how the measured IPRF affects aperture photometry for a range of motions of stars across the CCD pixels.

For simulations with drift, PSF positions are also randomly selected from a Gaussian jitter distribution, but the mean of the distribution is moved in incremental steps across the pixel for each exposure. For drift models, the jitter distribution with $\sigma = 0.06$ pixels was used. We have simulated observations with drift across half of a pixel, as well as across a full pixel width to study how different amounts of drift affect the resulting photometry. Examples of selected PSF locations with different jitter magnitudes and with and without drift are shown in figure 27.

For each magnitude, observations for five different stars with jitter distributions centered on different areas of the pixel were simulated. This was done to account for the fact that the IPRF varies across the pixel and is not perfectly symmetric. Depending

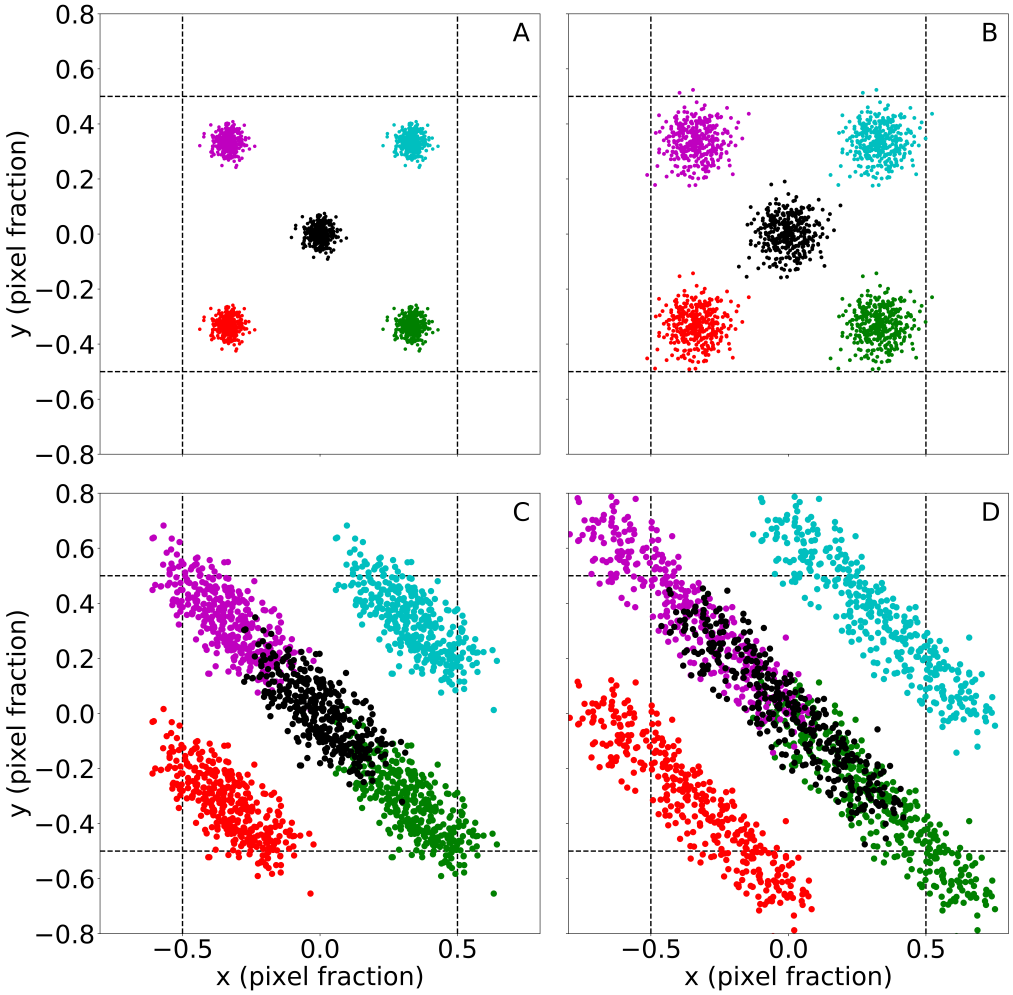


Figure 27: Examples of Gaussian jitter distributions with $\sigma = 0.03$ pixels (upper left) and $\sigma = 0.06$ pixels (upper right) and modeled drift across half of the pixel width (bottom left) and a full pixel width (bottom right). For models with drift, a jitter distribution with $\sigma = 0.06$ pixels is used.

on where a star is located on the pixel, the IPRF will affect the resulting photometry differently. In actual photometry, stars can be centered at any point within a pixel, so we account for stars located in multiple regions of the pixel to accurately model how the IPRF will affect real photometric measurements of many stars. The results presented in section 7.3 are the average results of all five positions modeled.

## 7.2 Aperture Selection

To select apertures, *Kepler* used a method in which an ideal aperture for each target was determined based on individual pixel SNR as well as overall aperture SNR. These

ideal apertures could be any size or shape;[21,61] however, *Kepler* can only store a limited number of apertures on board, so the stored aperture that was a best match to the ideal aperture was used for each target. Ideal apertures for each target star were computed each quarter. These apertures were selected to maximize the SNR for the aperture photometry to obtain the best photometric precision possible.

For our general aperture photometry analysis we use simple "circular" apertures, without fractional pixels. For the purposes of this discussion, we define an *observation set* to mean the set of all images for an individual star. An observation set is defined by the magnitude and pixel location of the star, as well as the observing conditions modeled for the observation (i.e. the amount of spacecraft jitter and/or drift modeled). For example, each different group of dots in each different plot in figure 27 belong to different observation sets.

The aperture size for each observation set is selected to maximize the SNR of the aperture photometry of the whole set. The average value of the total estimated flux within the aperture for each frame is used as the signal value, and the standard deviation about this mean is used as the noise value; the reason we use this value for the noise is discussed in detail in section 7.2.2. This is calculated for a range of aperture radii, and the radius resulting in the maximum SNR is selected; this is discussed further in section 7.2.3. Because of the way the SNR is calculated, *all images for a given observation set will have the same aperture size*, but the aperture size can vary from observation set to observation set. Although the aperture size is the same for all images in a set, in situations where spacecraft jitter or drift result in the star being centered on different pixels, the aperture is allowed to move to be centered on the same pixel as the star.

In general, the same aperture size is selected for all observation sets modeled under the same observing conditions, regardless of the location of the observation set within a pixel. We found that the main factors resulting in the selection of different aperture sizes were 1) the magnitude of the star, larger aperture sizes are selected for brighter stars; and 2) whether or not drift is part of the model. In some cases, observation sets modeled with drift result in a larger aperture being selected than for sets of the same magnitude without drift. The rest of this subsection is dedicated to a detailed discussion of how we select apertures for each observation set, and why we use this method for aperture selection.

### 7.2.1 Growth Curve Analysis

We have calculated growth curves for models with a perfectly uniform IPRF, as well as the measured *Kepler* IPRF. Growth curves for simulated data of a star located at the center of a pixel and a star located at the corner of a pixel are shown in figure 28. All curves have been peak normalized and the scale is given as the % of the detectable signal enclosed. Because the modeled PSF is the same for all simulated stars, *the growth curves shown are the same for all stars located in the same region of the pixel at all magnitudes.* No major differences in the growth curves for stars located in different corners of the pixel were observed, so the growth curve for only one corner is shown.

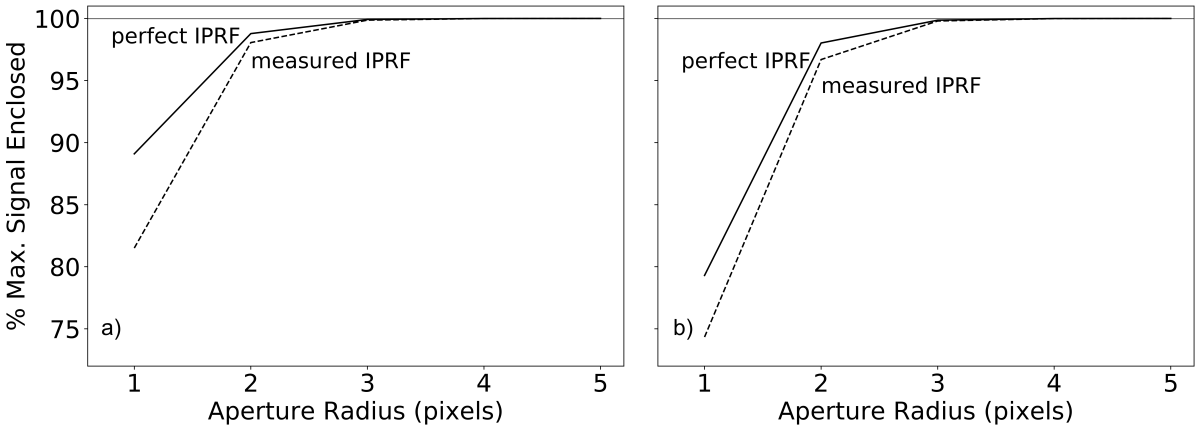


Figure 28: a) Growth curves showing the percent of the maximum signal enclosed for increasing aperture radii for stars located near the center of a pixel modeled with a perfect IPRF and the measured IPRF. b) Growth curves for stars located near the corner of a pixel modeled with a perfect IPRF and the measured IPRF. The shape of the growth curves varies for small radii, but in all cases the maximum detectable signal is collected at a radius of about 3 pixels.

The shape of the growth curves for stars located near the center of the pixel is slightly different than the growth curves for stars located near the edges for small radii, but both reach the maximum detectable signal at an aperture radius of ∼3-4 pixels. For small apertures, less light is detected for stars near the edges of the pixel than for stars near the pixel center. Apertures for radius $r = 1$ to $r = 4$ pixels are shown in figure 29. For an aperture of radius $r = 1$ pixel, the aperture will be 5 pixels in area in a "plus" shape centered on the brightest pixel. Figure 26a shows the binned PSF of a star centered on the middle of a pixel, and figure 26b shows the binned PSF of a star centered near the upper right corner of the central pixel. Due to the asymmetric spread of the signal with respect to the brightest pixel for star b, the signal present in

the $r = 1$ pixel aperture for this star would be significantly less than the signal present in the aperture for the centered star. As the aperture radius increases, this asymmetry has less of an effect on the aperture sum.

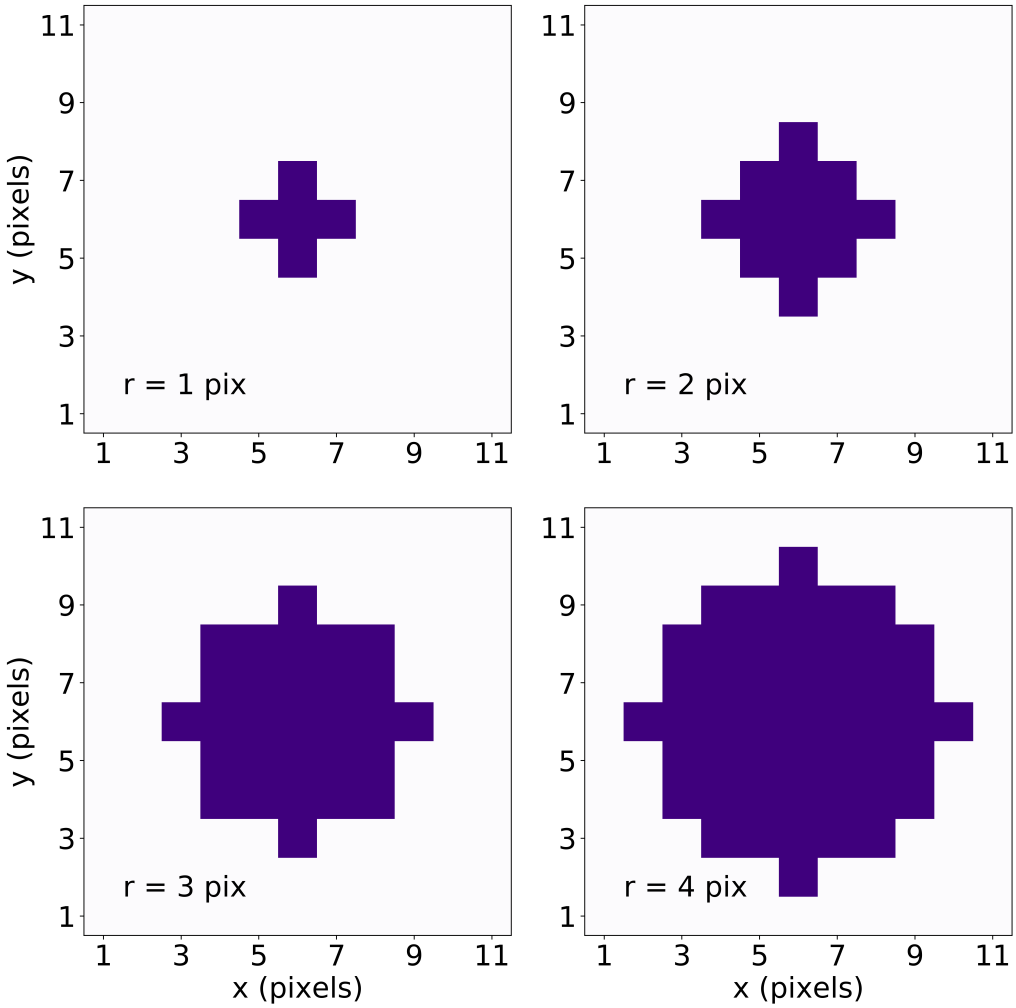


Figure 29: Apertures for radii r = 1 pixel to r = 4 pixels. Apertures are always centered on the same pixel as the PSF.

Also for apertures with small radii, the signal contained within the aperture is larger for observations using the perfect IPRF than observations using the measured IPRF. With a perfect IPRF it is assumed that the pixel response is uniform across the entire pixel, and that there is no diffusion into neighboring pixels. The decrease in signal observed when the measured IPRF is used is due to diffusion into pixels that are located outside of the aperture, which does not occur when a perfect IPRF is assumed. This effect quickly diminishes with increasing aperture radius, and for both types of IPRF

the maximum detectable signal is collected at the same aperture size.

From these growth curves, it was determined that any annulus with an inner radius equal to, or larger than, 4 pixels would give an accurate background measurement. This growth curve analysis along with analysis of SNR curves, indicated that using an annulus with an inner radius 6 pixels larger than the chosen aperture radius and a thickness of 5 pixels was ideal. Even for the smallest apertures selected, this annulus selection method results in an annulus that does not include significant amounts of light from our star. Also, since there are no other stars in our simulated images, we do not need to worry about other sources contaminating the background signal in our annulus when large apertures, and therefore large annuli, are selected.

Growth curves cannot, on their own, be used to determine the ideal aperture size for each set of observations. Instead, they must be analyzed along with the raw aperture photometry results for each image in the set and SNR curves. The raw aperture photometry results (shown and discussed in section 7.2.2) reveal systematic trends in the data that are not obvious from growth curves alone. Also, as mentioned in section 2.3, the goal of aperture photometry in exoplanet search missions is to maximize the SNR of the time-series photometry, so SNR curves must be taken into account when determining aperture size.

### 7.2.2 Systematic Effects Observed in Raw Aperture Photometry Results

When choosing the proper aperture size, one of the main goals is to mitigate systematic effects while retaining the highest SNR possible. Figure 30 shows the total flux within the aperture for observations with half pixel drift using a perfect IPRF (left) and the measured IPRF (right) for stars with magnitude Kp = 12.0. Each point in the plots is the aperture photometry result of a single image. The top row shows the result of using an aperture with radius $r = 2$ pixels, and the bottom plots use an aperture of $r = 3$ pixels. For all plots shown, the star is located near the corner of the pixel at the beginning of the observation, drifts through the center of the pixel, and ends near the corner diagonal from the starting position.

When the aperture size is too small, drift creates strong trends in the observed data. In figure 30 this is seen as an arc in the $r = 2$ pixel plots. The peak of this arc corresponds to the point at which the star is located near the center of the pixel. In this case, the standard deviation of the aperture sums about the mean ($\sigma$) is strongly influenced by this trend, making it much larger than the uncertainty calculated for a

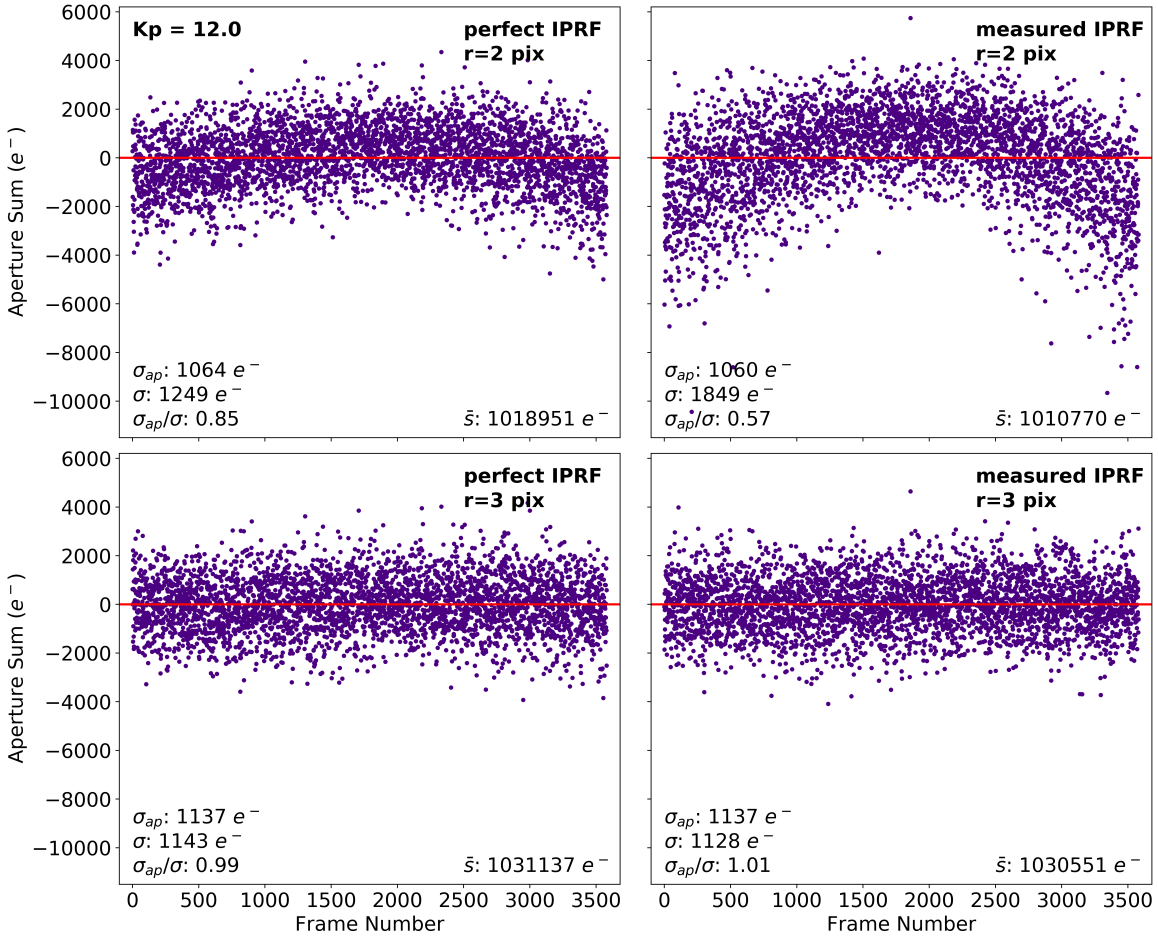


Figure 30: Raw aperture photometry results for four observation sets for Kp = 12.0 stars. Dots are the total estimated flux within the aperture for each image. Each plot has had its mean set as the zero value so the spread in the points can be easily compared. All plots are shown on the same y-scale. $\sigma_{ap}$ is the calculated uncertainty in a single point, $\sigma$ is the standard deviation about the mean for all points in the observation set, $\bar{s}$ gives the mean flux within the aperture for the whole set.

single aperture photometry measurement ($\sigma_{ap}$). The systematic effects due to drift are exacerbated when the measured IPRF is used, as is evident by the more pronounced arc in the upper right plot. Selecting this aperture size for this observation would result in drift having a large effect on the resulting photometric precision, a situation we would like to avoid.

By increasing the aperture radius (bottom row), these systematic effects can be mitigated. The increased aperture size results in much less light being "lost" when the star is centered near the edges of the central pixel compared to the middle because

much less light is present in the PSF at this distance from the center, so small changes in location have less of an effect on the total signal within the aperture. This results in a much flatter light curve for which the standard deviation of the aperture sums about the mean reflects the scatter in the points, not the trend due to drift. In this case, $\sigma$ less than in the previous case and is approximately equal to the uncertainty in a single aperture sum $\sigma_{ap}$. Any effects due to drift on the resulting photometric precision are mitigated by this increase in aperture size.

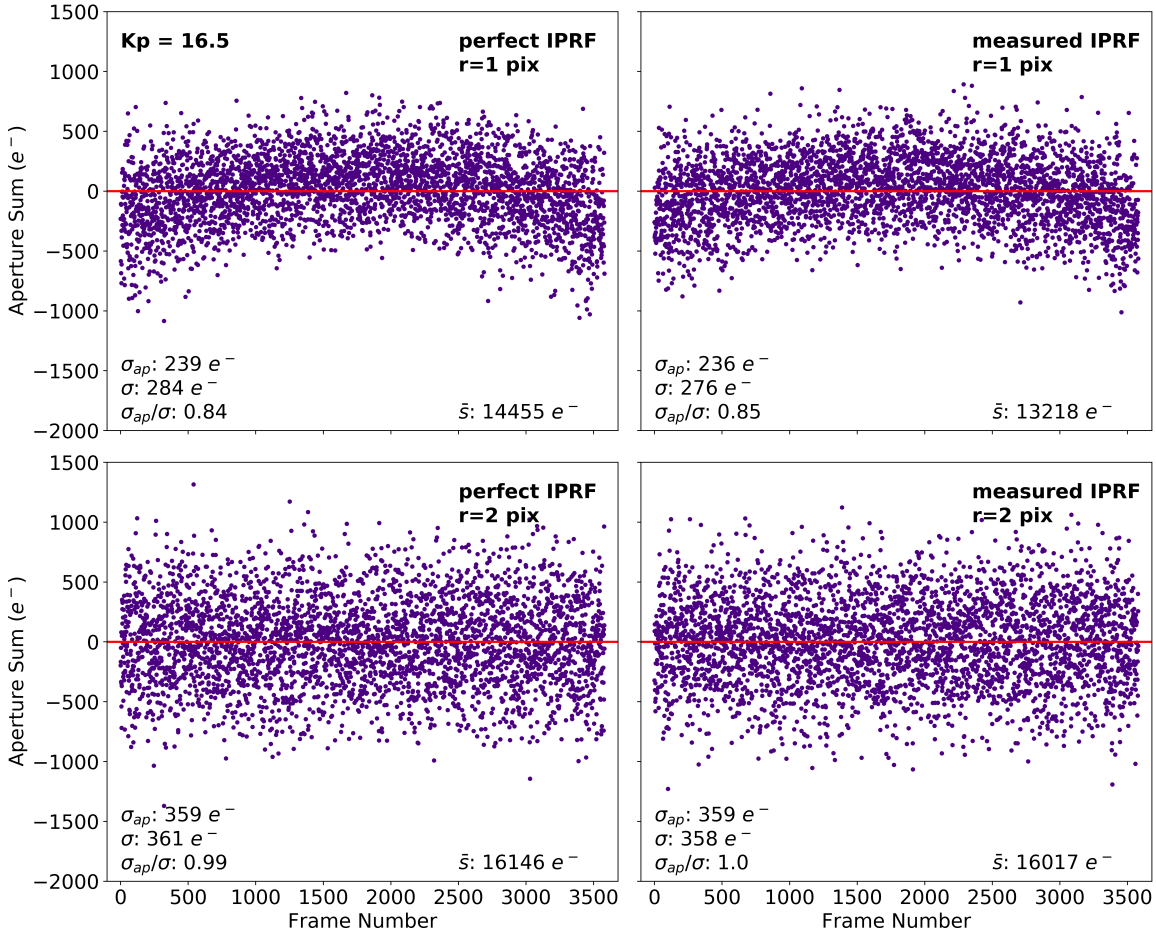


Figure 31: Raw aperture photometry results for four observation sets for Kp = 16.5 stars. Dots are the total estimated flux within the aperture for each image. Each plot has had its mean set as the zero value so the spread in the points can be easily compared. All plots are shown on the same y-scale. $\sigma_{ap}$ is the calculated uncertainty in a single point, $\sigma$ is the standard deviation about the mean for all points in the observation set, $\bar{s}$ gives the mean flux within the aperture for the whole set.

For larger apertures, drift contributes even less to the overall uncertainty, but the

increase in read noise causes the overall SNR to begin to decrease rapidly with increasing aperture radius; this is discussed further in section 7.2.3. The key goal of our aperture selection method is to mitigate systematic effects as much as possible, while maintaining the highest SNR possible for the observation set in question. This becomes more difficult for faint stars because read noise becomes problematic at smaller radii.

Figure 31 shows the raw aperture photometry results for stars with magnitude Kp=16.5 using apertures with radius $r = 1$ pixel (top row) and $r = 2$ pixels (bottom row). In this case, the trend due to drift is again observed for the smaller aperture, and is not present in the results of the aperture photometry using a larger aperture. However, increasing the aperture radius in this case increases the standard deviation about the mean quite a bit. In these cases, the aperture with the highest SNR is selected, even if there are still systematic effects in the data. As a result, the photometric precision for faint stars will be affected more by these systematics due to a smaller aperture size being selected to maintain the highest SNR possible. This is not ideal and we try to avoid this wherever possible; however, in missions like *Kepler* these effects can often still be mitigated after the fact using differential aperture photometry and detrending.

### 7.2.3 SNR Curves

The size of the aperture used for each set of observations is selected to be the radius at which the SNR is highest. In many cases, this selection method mitigates the systematic effects discussed in section 7.2.2, but is less effective at decreasing these effects for fainter stars. Example SNR curves are shown in figure 32. These plots each show three curves, 1) the SNR curve using the individual aperture uncertainty; 2) the SNR for simulated observations with a perfectly uniform IPRF; 3) the SNR for simulated observations with the measured IPRF. Curve 3 (solid black) is the curve used to determine the aperture radius for each observation set in our model. For the uncertainty calculation of the aperture photometry of individual frames, the only noise sources considered are shot noise and read noise. Curves 2 and 3 use the standard deviation about the mean of the individual aperture flux measurements to calculate the SNR.

Data points for $r = 2$ and $r = 3$ pixels in figure 32b correspond to the the raw aperture photometry results shown in figure 30. The data points in figure 32b for $r = 2$ pixels correspond to the top row of figure 30, and the points at r = 3 pixels correspond to the data shown in the bottom row of figure 30. The SNR calculated using the uncertainty in a single aperture ($\sigma_{ap}$ in figure 30) peaks at $r = 2$ pixels; however, at

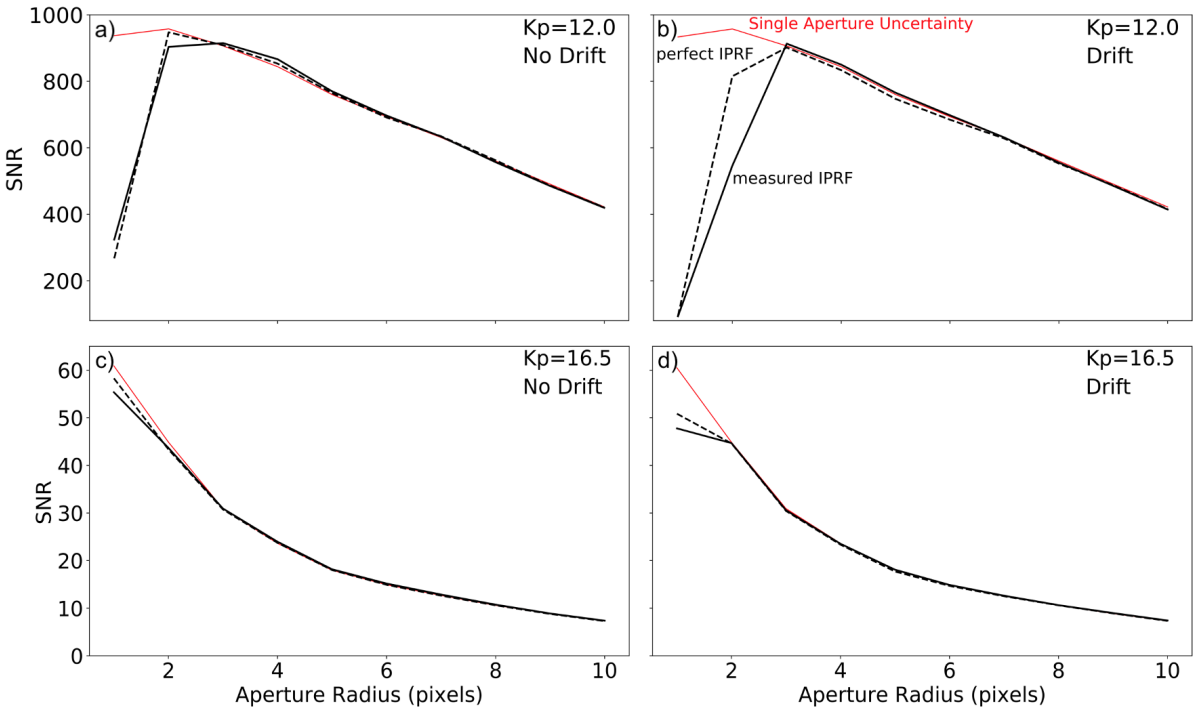


Figure 32: The SNR curves for stars with magnitude Kp = 12.0 (top) and Kp = 16.5 (bottom) without drift (left) and with drift (right).

this radius the systematic effects due to drift still have a large influence on $\sigma$ as shown in the raw photometry results plot, causing the SNR calculated using this value to be much lower.

The SNR curve for the measured IPRF in 32b peaks at $r = 3$ pixels (where $\sigma \approx \sigma_{ap}$), and the effects due to drift are mitigated as shown in figure 30. If the aperture size were to be selected based on the single aperture SNR, systematics such as pointing drift would have a significant effect on the resulting photometric precision. Using the aperture size corresponding to the peak of the measured IPRF SNR curve reduces the systematic effects on the resulting photometric precision, and maximizes the SNR of the ensemble of measurements in the set. The same is true for the observations with no drift shown in figure 32a, but for all aperture radii in this case the systematic effects are not as significant.

For fainter stars, the same selection method is used, but as is evident in the bottom row plots of figure 32, the individual aperture SNR peaks at the same radius as the ensemble SNR and $\sigma \neq \sigma_{ap}$ at this radius. In these cases, an aperture with radius $r = 1$ pixel is chosen based on the SNR curve, but as shown in figure 31, systematic

effects will still be significant using this aperture size. This will result in spacecraft jitter and drift having a larger effect on the photometric precision of faint stars than bright stars.

In general for our model, larger apertures are selected for brighter stars, and at certain magnitudes larger apertures are selected for observations with drift than for observations with only jitter. Using the method described here, our selected apertures range in size from $r = 1$ pixels (5 pixels in area) for the dimmest stars with no drift, to $r = 3$ pixels (29 pixels in area) for the brightest stars when drift is included in the model. Depending on the aperture size used, we expect systematic effects to be more or less evident in the resulting photometric precision.

## 7.3 Effects on Photometric Precision Due to IPRF

To determine the effects of the measured IPRF on aperture photometry, we plot the photometric precision achieved at each magnitude under different observing conditions. The photometric precision in parts per million at a given *Kepler* magnitude is defined as:

$$p = \frac{\sigma_S}{\sqrt{N} \times S_{avg}} \times 10^6 \tag{8}$$

where $p$ is the photometric precision in parts-per-million, $\sigma_S$ is the standard deviation about the mean for all aperture flux measurements in an observation set, $N$ is the number of reads performed in the set, and $S_{avg}$ is the average signal in an aperture after background subtraction.

Figure 33 shows the photometric precision for all of the observation conditions modeled using a perfectly uniform IPRF. The curve labeled "perfect IPRF" shows the result of observations modeled with no spacecraft jitter or drift using a perfect IPRF and is considered the baseline, or the best possible precision that could be achieved with no systematic effects. Deviations from the noise limit for this curve are due to the placement of the five modeled stars across the pixel. For apertures with small radii, as is the case for faint stars, stars located near the corner of the central pixel result in less light being recorded in the aperture than for a star located at the center of the pixel as shown by the growth curve plots in figure 28. This adds some noise to the average measurement that is not accounted for in the calculated noise limit.

As expected, the systematic effects due to a stars movement across a pixel are larger for fainter stars because of the aperture size used as discussed in previous sections,

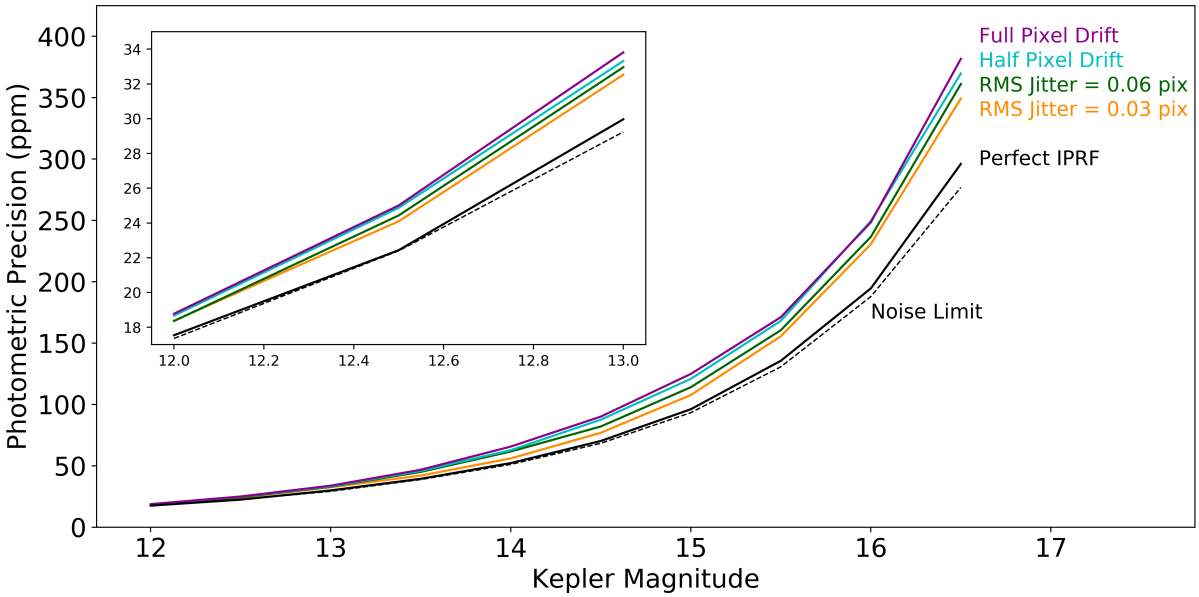


Figure 33: Photometric precision averaged over all PSF locations using a perfect IPRF in the model.

but there are still observable effects for the brightest stars as shown in the inset plot in figure 33. For all magnitudes, the more a star moves across a pixel during an observation, the larger the observed effects on the aperture photometry are.

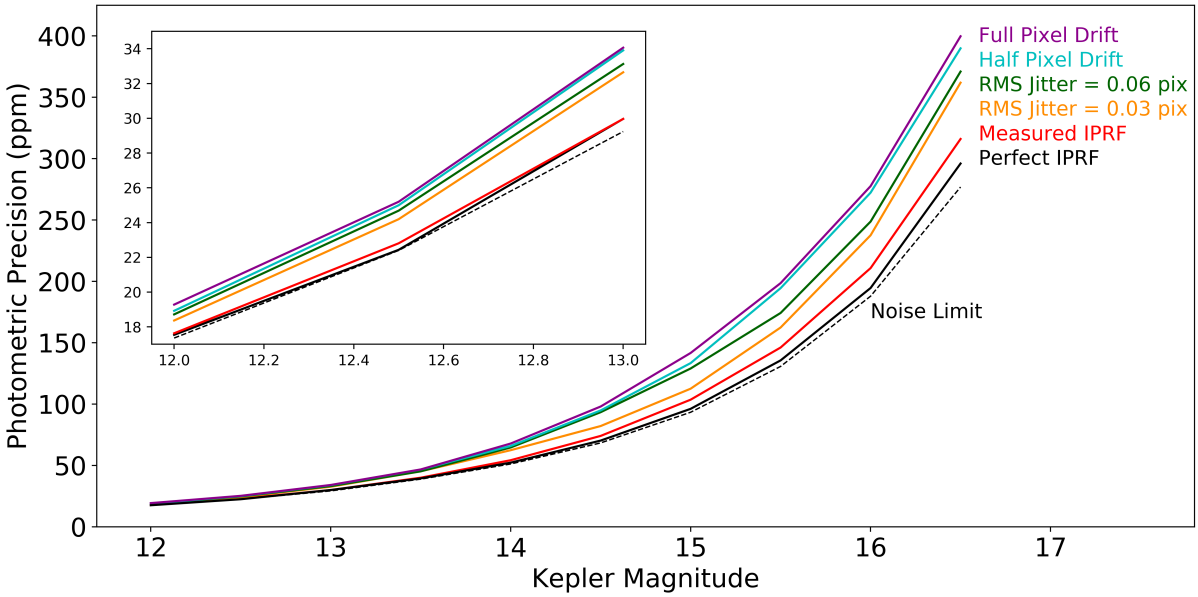


Figure 34: Photometric precision averaged over all PSF locations for observations using the measured IPRF in the model.

To observe the effects of the IPRF in each of these cases, we compare figure

33 to figure 34 which shows the photometric precision for observations with the same conditions, but which include the measured IRPF in the model. The same systematic effects present in the plot without the measured IPRF are still present in this plot, but any decrease in photometric precision from figure 33 to figure 34 is due to the measured IPRF. The scale of the y-axis is the same for both plots to allow for easy comparison.

In all cases and at all magnitudes, the measured IPRF causes a decrease in photometric precision. Similar to the other systematic effects, the effect due to the measured IPRF is larger for faint stars than for bright stars. The measured IPRF also has a larger effect on the photometric precision of observations modeled with drift than on observations modeled without drift. In general, the more a star moves across a pixel, the larger the effect due to the IPRF will be, and the more important it is to account for these sub-pixel sensitivity variations.

Current exoplanet search missions such as *Kepler* and TESS attempt to account for sub-pixel sensitivity variations without *a priori* knowledge of the IPRF through detrending. However, knowledge of the IPRF can be used to improve these methods and further mitigate systematic effects on photometry. This could be even more useful for TESS than for *Kepler* because the TESS passband is shifted further into the red where we observe more structure in the IPRF, and the mission focuses on fainter stars for which these effects are more significant.

# 8. CONCLUSIONS

## 8.1 IPRF Measurement

The IPRF of a back-illuminated e2v CCD90, the same CCD model used in the *Kepler* mission, was measured for wavelengths across the *Kepler* spectral band. The measurements show strong wavelength dependence, with more diffusion being observed for shorter wavelengths, and small-scale structure present at longer wavelengths. These results show good agreement with previous studies of other back-illuminated CCDs.

Also, a method was suggested for creating an effective IPRF which can be applied to *Kepler* data, which depends on the spectrum of the star being observed as well as the *Kepler* response curve.

The temperature dependence of the IPRF was considered, and it was found that the 40°C temperature difference between the CCD we used to measure the IPRF and the CCDs on board the *Kepler* Space Telescope should not have a significant effect on the effective IPRF.

## 8.2 Sub-pixel QE Variations

Sub-pixel variations in QE were measured by performing aperture photometry on spot scan images. These variations were found to be wavelength dependent, with variations across a pixel ranging from about 2% to 7%. The structure of the QE variations followed a similar trend with wavelength as the IPRF structure, with the variations at shorter wavelengths being more uniform, and long wavelengths showing small scale structure indicating interactions with the gate structure. We expect that at least some of the variation observed at long wavelengths is due to reflections off the gates.

## 8.3 Simulated Aperture Photometry

A model was created to study the effects of the measured IPRF on aperture photometry. Observations were simulated for stars ranging from Kp = 12.0 to Kp = 16.5 corresponding to about 6.5 hrs of *Kepler* observations. The model has been kept simple, accounting only for the measured IPRF, spacecraft jitter, pointing drift, shot noise and read noise.

Aperture photometry was performed on these simulated images using circular apertures with sizes selected to maximize the SNR for all measurements in an observation set. For bright stars, this selection method mitigates systematic effects that are observed

in apertures with small radii, but for faint stars small radii are selected resulting in significant systematic effects on the resulting photometric precision.

Comparing observations made assuming a perfect IPRF in the model with observations made using the measured IPRF in the model, it was found that the effects due to the IRPF are more significant for dimmer stars, but a decrease in photometric precision was observed at all magnitudes. It was also found that as the amount of movement of a star across a pixel during an observation set is increased, the effects of the measured IPRF on the resulting aperture photometry also increase, and it is more important to account for sub-pixel sensitivity variations.

# 9. FUTURE WORK

## 9.1 Effects of Sub-pixel QE Variations and Simulated *Kepler* Photometry

The current aperture photometry model takes into account the measured IPRF, but does not account for the sub-pixel QE variations observed. Moving forward, the measured variations in sub-pixel QE will be included in the simulated photometry model. Also, a more sophisticated model will be developed to specifically model *Kepler* data instead of the general analysis provided here. This model will be used to study the effects introduced by the measured IPRF and sub-pixel QE variations on *Kepler* data specifically, and to develop methods to correct these effects.

## 9.2 Determination of the Optical PSF

One of the main purposes of directly measuring the *Kepler* IPRF is to use the measurement to determine the optical PSF of the telescope, which up to this point is unknown. Knowledge of the precise optical PSF will allow for PSF fitting to be used to perform photometry on *Kepler* data. This method has many advantages over aperture photometry, especially in crowded fields, and could result in significant improvements to data analysis.

## Acknowledgements

I would like to thank Dr. Zoran Ninkov for advising me through the completion of this thesis. I would also like to thank Dr. Dmitry Vorobiev for all of his help and contributions to this research. Thank you also to Dr. Kevan Donlon for assisting with the development of data processing procedures for the IPRF measurement. Finally, I would like to thank Dr. Zoran Ninkov, Dr. Dmitry Vorobiev, and Dr. Joel Kastner for serving on my Master's committee.

# REFERENCES


[1] L., W., "Ptolemy as a philosopher and astrologer," *Nature* **50**, 398 – 399 (1894).

[2] Miles, R., "A light history of photometry: from Hipparchus to the Hubble Space Telescope," *Journal of the British Astronomical Association* **117**, 172–186 (Aug. 2007).

[3] Pritchard, C., [*Uranometria Nova Oxoniensis: A Photometric Determination of the Magnitudes of all Stars Visible to the Naked Eye from the Pole to Ten Degrees South of the Equator*], Oxford University Press (1885).

[4] Cousins, A. W. J., "Some Methods of Stellar Photometry," *Monthly Notes of the Astronomical Society of South Africa* **8**, 95 (Jan. 1949). Provided by the SAO/NASA Astrophysics Data System.

[5] Janesick, J., [*Scientific Charge-coupled Devices*], SPIE Press Monograph Series, SPIE (2001).

[6] Braddick, H. J. J., "Photoelectric photometry," *Reports on Progress in Physics* **23**, 154–175 (jan 1960).

[7] McLean, I. S., [*Electronic Imaging in Astronomy*], Wiley-Praxis Series in Astronomy and Astrophysics, John Wiley & Sons Ltd in association with Praxis Publishing Ltd, Chichester, UK (1997).

[8] O'Donoghue, D., "High Speed CCD Photometry," *Baltic Astronomy* **4**, 519–526 (Jan. 1995).

[9] Gilliland, R. L., Chaplin, W. J., Dunham, E. W., Argabright, V. S., Borucki, W. J., Basri, G., Bryson, S. T., Buzasi, D. L., Caldwell, D. A., Elsworth, Y. P., Jenkins, J. M., Koch, D. G., Kolodziejczak, J., Miglio, A., van Cleve, J., Walkowicz, L. M., and Welsh, W. F., "Kepler Mission Stellar and Instrument Noise Properties," *ApJS* **197**, 6 (Nov. 2011).

[10] Vanderspek, R., Doty, J. P., Fausnaugh, M., Villasenor, J. N. S., Jenkins, J. M., Berta-Thompson, Z. K., Burke, C. J., and Ricker, G. R., *TESS Instrument Handbook* (2018).

[11] Howell, S. B., "Two-Dimensional Aperture Photometry: Signal-to-Noise Ratio of Point-Source Observations and Optimal Data-Extraction Techniques," *PASP* **101**, 616 (June 1989).

[12] Stetson, P. B., "On the Growth-Curve Method for Calibrating Stellar Photometry with CCDs," *textit* **102**, 932 (Aug. 1990).

[13] HOWELL, S. B. and JACOBY, G. H., "Time-resolved photometry using a ccd," *Publications of the Astronomical Society of the Pacific* **98**(606), 802–808 (1986).

[14] Howell, S. B., Mitchell, K. J., and Warnock, A., I., "Statistical error analysis in CCD time-resolved photometry with applications to variable stars and quasars.," **95**, 247–256 (Jan. 1988).

[15] Rowe, J. F., Bryson, S. T., Marcy, G. W., Lissauer, J. J., Jontof-Hutter, D., Mullally, F., Gilliland, R. L., Issacson, H., Ford, E., Howell, S. B., Borucki, W. J., Haas, M., Huber, D., Steffen, J. H., Thompson, S. E., Quintana, E., Barclay, T., Still, M., Fortney, J., Gautier, T. N., Hunter, R., Caldwell, D. A., Ciardi, D. R., Devore, E., Cochran, W., Jenkins, J., Agol, E., Carter, J. A., and Geary, J., "Validation of Kepler's Multiple Planet Candidates. III. Light Curve Analysis and Announcement of Hundreds of New Multi-planet Systems," *The Astrophysical Journal* **784**, 45 (mar 2014).

[16] Howell, S., [*Handbook of CCD Astronomy*], Cambridge Observing Handbooks for Research Astronomers, Cambridge University Press (2006).

[17] Da Costa, G. S., "Basic Photometry Techniques," in [*Astronomical CCD Observing and Reduction Techniques*], Howell, S. B., ed., *Astronomical Society of the Pacific Conference Series* **23**, 90 (Jan. 1992).

[18] Lauer, T. R., "Combining Undersampled Dithered Images," **111**, 227–237 (Feb. 1999).

[19] Lauer, T., "The photometry of undersampled point-spread functions," *Publications of the Astronomical Society of the Pacific* **111**(765), 1434–1443 (1999).

[20] Bryson, S. T., Tenenbaum, P., Jenkins, J. M., Chandrasekaran, H., Klaus, T., Caldwell, D. A., Gilliland, R. L., Haas, M. R., Dotson, J. L., Koch, D. G., and Borucki, W. J., "THE KEPLER PIXEL RESPONSE FUNCTION," *The Astrophysical Journal* **713**, L97–L102 (mar 2010).

[21] Van Cleve, J. E. and Caldwell, D. A., "Kepler instrument handbook," Tech. Rep. KSCI-19033-002, NASA Ames Research Center, Moffett Field, CA (2016).

[22] Twicken, J. D., Clarke, B. D., Bryson, S. T., Tenenbaum, P., Wu, H., Jenkins, J. M., Girouard, F., and Klaus, T. C., "Photometric analysis in the Kepler Science Operations Center pipeline," in [*Software and Cyberinfrastructure for Astronomy*], Radziwill, N. M. and Bridger, A., eds., **7740**, 749 – 760, International Society for Optics and Photonics, SPIE (2010).

[23] Aigrain, S., Hodgkin, S. T., Irwin, M. J., Lewis, J. R., and Roberts, S. J., "Precise time series photometry for the Kepler-2.0 mission," *Monthly Notices of the Royal Astronomical Society* **447**, 2880–2893 (01 2015).

[24] Ricker, G. R., Winn, J. N., Vanderspek, R., Latham, D. W., Bakos, G. , Bean, J. L., Berta-Thompson, Z. K., Brown, T. M., Buchhave, L., Butler, N. R., Butler, R. P., Chaplin, W. J., Charbonneau, D. B., Christensen-Dalsgaard, J., Clampin, M., Deming, D., Doty, J. P., Lee, N. D., Dressing, C., Dunham, E. W., Endl, M., Fressin, F., Ge, J., Henning, T., Holman, M. J., Howard, A. W., Ida, S., Jenkins, J. M., Jernigan, G., Johnson, J. A., Kaltenegger, L., Kawai, N., Kjeldsen, H., Laughlin, G., Levine, A. M., Lin, D., Lissauer, J. J., MacQueen, P., Marcy, G., McCullough, P. R., Morton, T. D., Narita, N., Paegert, M., Palle, E., Pepe, F., Pepper, J., Quirrenbach, A., Rinehart, S. A., Sasselov, D., Sato, B., Seager, S., Sozzetti, A., Stassun, K. G., Sullivan, P., Szentgyorgyi, A., Torres, G., Udry, S., and Villasenor, J., "Transiting Exoplanet Survey Satellite," *Journal of Astronomical Telescopes, Instruments, and Systems* **1**(1), 1 – 10 (2014).

[25] Jenkins, J. M., Twicken, J. D., McCauliff, S., Campbell, J., Sanderfer, D., Lung, D., Mansouri-Samani, M., Girouard, F., Tenenbaum, P., Klaus, T., Smith, J. C., Caldwell, D. A., Chacon, A. D., Henze, C., Heiges, C., Latham, D. W., Morgan, E., Swade, D., Rinehart, S., and Vanderspek, R., "The TESS science processing operations center," in [*Software and Cyberinfrastructure for Astronomy IV*], Chiozzi, G. and Guzman, J. C., eds., **9913**, 1232 – 1251, International Society for Optics and Photonics, SPIE (2016).

[26] Feinstein, A. D., Montet, B. T., Foreman-Mackey, D., Bedell, M. E., Saunders, N., Bean, J. L., Christiansen, J. L., Hedges, C., Luger, R., Scolnic, D., and de Miranda Cardoso, J. V., "eleanor: An open-source tool for extracting light curves from the TESS full-frame images," *Publications of the Astronomical Society of the Pacific* **131**, 094502 (jul 2019).

[27] Boyle, W. S. and Smith, G. E., "Charge coupled semiconductor devices," *The Bell System Technical Journal* **49**, 587–593 (April 1970).

[28] Amelio, G. F., Tompsett, M. F., and Smith, G. E., "Experimental verification of the charge coupled device concept," *The Bell System Technical Journal* **49**, 593–600 (April 1970).

[29] Jorden, P. R., Deltorn, J.-M., and Oates, A. P., "Nonuniformity of CCDs and the effects of spatial undersampling," in [*Instrumentation in Astronomy VIII*], Crawford, D. L. and Craine, E. R., eds., **2198**, 836 – 850, International Society for Optics and Photonics, SPIE (1994).

[30] Kavaldjiev, D. and Ninkov, Z., "Experimental measurement of the variation in sensitivity within a single pixel of a CCD," in [*Solid State Sensor Arrays: Development and Applications*], Blouke, M. M., ed., **3019**, 42 – 49, International Society for Optics and Photonics, SPIE (1997).

[31] Kavaldjiev, D. and Ninkov, Z., "Subpixel sensitivity map for a charge-coupled device," *Optical Engineering* **37**(3), 948 – 954 (1998).

[32] Kavaldjiev, D. and Ninkov, Z., "Influence of non-uniform charge-coupled device pixel response on aperture photometry," *Optical Engineering* **40**(2), 162 – 169 (2001).

[33] Piterman, A. and Ninkov, Z., "Measurements of the subpixel sensitivity for a backside-illuminated CCD," in [*Sensors and Camera Systems for Scientific, Industrial, and Digital Photography Applications*], Sampat, N., Yeh, T., Blouke, M. M., Sampat, N., Jr., G. M. W., and Yeh, T., eds., **3965**, 289 – 297, International Society for Optics and Photonics, SPIE (2000).

[34] Piterman, A. and Ninkov, Z., "Effect of nonuniform CCD pixel sensitivity variations on measurement accuracy," in [*Sensors and Camera Systems for Scientific, Industrial, and Digital Photography Applications II*], Sampat, N., Canosa, J., Blouke, M. M., Canosa, J., and Sampat, N., eds., **4306**, 280 – 288, International Society for Optics and Photonics, SPIE (2001).

[35] Piterman, A. and Ninkov, Z., "Subpixel sensitivity maps for a back-illuminated charge-coupled device and the effects of nonuniform response on measurement," *Optical Engineering* **41**(6), 1192 – 1202 (2002).

[36] Rajkanan, K., Singh, R., and Shewchun, J., "Absorption coefficient of silicon for solar cell calculations," *Solid-State Electronics* **22**(9), 793 – 795 (1979).

[37] O'Donnell, K. and Chen, X., "Temperature dependence of semiconductor band gaps," *Applied Physics Letters* **58**, 2924 – 2926 (07 1991).

[38] Toyozumi, H. and Ashley, M. C. B., "Intra-Pixel Sensitivity Variation and Charge Transfer Inefficiency — Results of CCD Scans," *Publications of the Astronomical Society of Australia* **22**(3), 257–266 (2005).

[39] Zhan, H., Zhang, X., and Cao, L., "Intrapixel effects of CCD and CMOS detectors," *Journal of Instrumentation* **12**, C04010–C04010 (apr 2017).

[40] Vorobiev, D., Ninkov, Z., Caldwell, D., and Mochnacki, S., "Direct measurement of the intra-pixel response function of the Kepler Space Telescope's CCDs," *Society of Photo-Optical Instrumentation Engineers (SPIE) Conference Series* **10698**, 106985J (July 2018).

[41] Vorobiev, D., Irwin, A., Ninkov, Z., Donlon, K., Caldwell, D., and Mochnacki, S., "Direct measurement of the Kepler Space Telescope CCD's intrapixel response function," *Journal of Astronomical Telescopes, Instruments, and Systems* **5**(4), 1 – 14 (2019).

[42] Mahato, S., De Ridder, J., Meynants, G., Raskin, G., and Van Winckel, H., "A novel technique to characterize the spatial intra-pixel sensitivity variations in a cmos image sensor," in [*2017 15th IEEE International New Circuits and Systems Conference (NEWCAS)*], 361–364 (June 2017).

[43] Mahato, S. B., de Ridder, J., Meynants, G., Raskin, G., and van Winckel, H., "Measuring intra-pixel sensitivity variations of a cmos image sensor," *IEEE Sensors Journal* **18**, 2722–2728 (April 2018).

[44] Ivory, J., Stefanov, K. D., Turner, P., and Holland, A. D., "PSF and non-uniformity in a monolithic fully depleted 4T CMOS image sensor," in [*High Energy, Optical, and Infrared Detectors for Astronomy VIII*], Holland, A. D. and Beletic, J., eds., **10709**, 568 – 576, International Society for Optics and Photonics, SPIE (2018).

[45] Penny, A. J. and Leese, R., "Stellar Photometry with CCD Sub-Pixel Sensitivity Variations," in [*Astronomical Data Analysis Software and Systems V*], Jacoby, G. H. and Barnes, J., eds., *Astronomical Society of the Pacific Conference Series* **101**, 29 (Jan. 1996).

[46] Holtzman, J. A., Hester, J. J., Casertano, S., Trauger, J. T., Watson, A. M., Ballester, G. E., Burrows, C. J., Clarke, J. T., Crisp, D., Evans, R. W., John S., I. G., Griffiths, R. E., Hoessel, J. G., Matthews, L. D., Mould, J. R., Scowen, P. A., Stapelfeldt, K. R., and Westphal, J. A., "The performance and calibration of WFPC2 on the huble space telescope," *Publications of the Astronomical Society of the Pacific* **107**, 156 (feb 1995).

[47] Abdelsalam, D. G., Stanislas, M., and Coudert, S., "Subpixel characterization of a PIV-CCD camera using a laser spot," *Measurement Science and Technology* **25**, 084006 (jul 2014).

[48] Abdelsalam, D. G., Stanislas, M., and Coudert, S., "CCD or CMOS camera calibration using point spread function," in [*International Conference on Experimental Mechanics 2013 and Twelfth Asian Conference on Experimental Mechanics*], Sirisoonthorn, S., ed., **9234**, 251 – 254, International Society for Optics and Photonics, SPIE (2014).

[49] Stanislas, M., Abdelsalam, D. G., and Coudert, S., "CCD camera response to diffraction patterns simulating particle images," *Appl. Opt.* **52**, 4715–4723 (Jul 2013).

[50] Biesiadzinski, T. P., Tarlé, G., Howe, M. J., Schubnell, M., Lorenzon, W., Weaverdyck, C., and Larson, J., "A method for the characterization of sub-pixel response of near-infrared detectors," in [*High Energy, Optical, and Infrared Detectors for Astronomy IV*], Holland, A. D. and Dorn, D. A., eds., **7742**, 497 – 505, International Society for Optics and Photonics, SPIE (2010).

[51] Barron, N., Borysow, M., Beyerlein, K., Brown, M., Lorenzon, W., Schubnell, M., Tarle, G., Tomasch, A., and Weaverdyck, C., "Subpixel Response Measurement of Near-Infrared Detectors," *Publications of the Astronomical Society of the Pacific* **119**, 466–475 (Apr. 2007).

[52] Ketchazo, C., Viale, T., Boulade, O., Druart, G., Moreau, V., Mugnier, L., Dubreuil, D., Derelle, S., Ronayette, S., Guérineau, N., and Berthe, M., "A new technique of characterization of the intrapixel response of astronomical detectors," in [*High Energy, Optical, and Infrared Detectors for Astronomy VI*], Holland, A. D. and Beletic, J., eds., **9154**, 634 – 647, International Society for Optics and Photonics, SPIE (2014).

[53] Hardy, T., Baril, M. R., Pazder, J., and Stilburn, J. S., "Intra-pixel response of infrared detector arrays for JWST," in [*High Energy, Optical, and Infrared Detectors for Astronomy III*], Dorn, D. A. and Holland, A. D., eds., **7021**, 711 – 722, International Society for Optics and Photonics, SPIE (2008).

[54] De Ridder, J., Arentoft, T., and Kjeldsen, H., "Modelling space-based high-precision photometry for asteroseismic applications," *Monthly Notices of the Royal Astronomical Society* **365**, 595–605 (01 2006).

[55] Paul, S., Goodenough, A. A., Brown, S. D., and Salvaggio, C., "Sub-pixel radiometry: a three-part study in generating synthetic imagery that incorporates sub-pixel variation," in [*Algorithms and Technologies for Multispectral, Hyperspectral, and Ultraspectral Imagery XVI*], Shen, S. S. and Lewis, P. E., eds., **7695**, 184 – 195, International Society for Optics and Photonics, SPIE (2010).

[56] O'Connor, P., Radeka, V., Figer, D., Geary, J. G., Gilmore, D. K., Oliver, J., Stubbs, C. W., Takacs, P. Z., and Tyson, J. A., "Study of silicon sensor thickness optimization for LSST," in [*High Energy, Optical, and Infrared Detectors for Astronomy II*], Dorn, D. A. and Holland, A. D., eds., **6276**, 546 – 559, International Society for Optics and Photonics, SPIE (2006).

[57] Bond, H. E. and Kim Quijano, J., "Wide field camera 3 instrument handbook, version 1.0," tech. rep., STScI, Baltimore, MD (2007).

[58] Howell, S. B., Koehn, B., Bowell, E., and Hoffman, M., "Detection and Measurement of Poorly Sampled Point Sources Imaged With 2-D Array," **112**, 1302 (Sept. 1996).

[59] Stumpe, M. C., Smith, J. C., Cleve, J. E. V., Twicken, J. D., Barclay, T. S., Fanelli, M. N., Girouard, F. R., Jenkins, J. M., Kolodziejczak, J. J., McCauliff, S. D., and Morris, R. L., "Kepler presearch data conditioning i—architecture and algorithms for error correction in kepler light curves," *Publications of the Astronomical Society of the Pacific* **124**, 985–999 (sep 2012).

[60] Knapp, M., Seager, S., Demory, B.-O., Krishnamurthy, A., Smith, M. W., Pong, C. M., Bailey, V. P., Donner, A., Pasquale, P. D., Campuzano, B., Smith, C., Luu, J., Babuscia, A., Robert L. Bocchino, J., Loveland, J., Colley, C., Gedenk, T., Kulkarni, T., Hughes, K., White, M., Krajewski, J., and Fesq, L., "Demonstrating high-precision photometry with a CubeSat: ASTERIA observations of 55 cancri e," *The Astronomical Journal* **160**, 23 (jun 2020).

[61] Jenkins, J. M., "Kepler data processing handbook," Tech. Rep. KSCI-19081-002, NASA Ames Research Center, Moffett Field, CA (2017).